NASA TECHNICAL MEMORANDUM 89099

STRENGTH OF A THICK GRAPHITE/EPOXY ROCKET MOTOR CASE AFTER IMPACT BY A BLUNT OBJECT

C. C. POE, JR. AND W. ILLG

FEBRUARY 1987

NASA
National Aeronautics and Space Administration
Langley Research Center
Hampton, Virginia 23665

INTRODUCTION

NASA is developing graphite/epoxy filament-wound cases (FWC) for the solid rocket motors of the space shuttle. Each motor consists of four cases -- a forward case, two center cases, and an aft case. The cases are 3.66 m (12 ft) in diameter and the ends are joined to short steel segments with pins. The forward and center cases are approximately 7.62 m (25 ft) in length, and the aft case is somewhat shorter. They are wet-wound with AS4W graphite fiber and HBRF-55A epoxy (Hercules Inc.). The membrane region away from the ends is about 36 mm (1.4 in.) thick.

A program was outlined in [1] for determining the effect of low-velocity impacts on the residual tension strength of a FWC. Initially, impact tests were conducted on thick aluminum beams of various lengths to determined how large a specimen was required. The results indicated that a 30-cm-long (12 in.) beam was long enough to simulate the dynamic behavior of a FWC. Thus, a 76.2-cm-diameter (25 ft), 2.13-meter-long (7 ft) cylinder of full-thickness was wet-wound to represent an aft segment of a FWC. In order to apply uniaxial load in the hoop direction (the most highly stressed direction in a pressurized cylinder) and have straight specimens, the cylinder was wound with fiber orientations rotated 90° so that the hoop direction of the FWC was the longitudinal direction of the cylinder. The cylinder was cut into seven 30.5-cm-long (12 in.) rings. Then a few specimens that were cut from several of the rings were impacted with impacters of various shapes. The shapes were 1.27-cm-radius (0.50 in.) and 0.635-cm-radius (0.25 in.) spheres, a 0.635-cm-diameter (0.25 in.) rod, and a 90° corner. The 1.27-cm-radius (0.50 in.) impacters made no visible surface damage, whereas the sharper impacters made visible craters. However, for a given kinetic energy, the residual strengths of the specimens were reduced about the same for the various impacters. Thus, impacts by the 1.27-cm-radius (0.50 in.) impacters were the most critical with regard to inspection.

Having identified the most critical impacter shape, two intact rings were then impacted 44 times each, every 5 cm (2 in.) of circumference, with the 1.27-cm-radius (0.50 in.) impacters. The purpose of the present paper is to summarize the results of these latter tests. The results are presented in more detail in [2]. One of the rings was empty and the other was filled with inert propellent. The propellent was cast into the ring, much like an actual FWC. The impacter masses varied from 2.8 to 18.6 kg (6.1 to 41.1 lbm) to represent tools and other heavy objects that might fall onto an FWC. They were dropped from heights varying from 0.38 to 3.0 m (1.2 to 10 ft) giving kinetic energies from 37.7 J (27.8 to 329 ft lbf). The impacters were instrumented to measure impact force. After the impacts, the rings were cut into 5.1-by-30.5-cm (2.0 by 12.0 in.) specimens. Each was centered on an impact site. The specimens were x-rayed and ultrasonically scanned to determine the extent of impact damage, and then loaded in uniaxial tension to measure the residual strength. A few specimens were deplied and the fibers were examined for impact damage. The conventional ultrasonic attenuation maps revealed no damage. In addition to the specimens with impacts, 16 specimens without impacts from two other rings were loaded to failure to determine how specimen width affected undamaged strength.

For low velocity impacts, it was suggested in [3,4,5] that the damage and resulting loss of strength depend on the maximum value of the impact force and the material characteristics. For this reason, the impact damage and residual strengths were analyzed here and in [2] in terms of impact force. Rigid body mechanics and the Hertz law were used to derive an equation for impact force in terms of kinetic energy and masses of the impacter and target. The depth of impact damage was predicted in terms of impact force using Love's solution for pressure applied on part of the boundary of a semi-infinite body and a principal shear stress criterion for failure. The Hertz law was used to predict the contact diameters and pressures that are required for Love's solution. The predicted and experimental values of damage depth were compared.

SYMBOLS

a	equivalent surface cut depth or impact damage depth, m (in.)
C_1, C_2	constants
D	contact diameter, m (in.)
E	Young's modulus, Pa (psi)
G	Shear modulus, Pa (psi)
k_f	spring constant for flexure, N/m (lbf/in.)
k_1,k_2	factors in the Hertz law, Pa^{-1} $(psi)^{-1}$
KE	kinetic energy, J (ft lbf)
$\tilde{KE}$	modified kinetic energy, J (ft lbf)
m_1	mass of impacter, kg (lbm)
m_2	mass of target or composite ring, kg (lbm)
$\tilde{m}_2$	effective mass of composite ring, kg (lbm)
n	factor in the Hertz law, $N^{3/2}m^{-3/2}$ $(lbf^{3/2}in.^{-3/2})$
P	maximum impact force, N (lbf)
p_c	average contact pressure, Pa (psi)
R_1	radius of impacter, m (in.)

S_c gross stress for failure of first ligament, Pa (psi)

S_u shear strength, Pa (psi)

t_o impact duration, sec

u_f flexural displacement, m (in.)

u_h Hertz displacement, m (in.)

v_1 velocity of impacter immediately before initial impact, m/sec (ft/sec)

v_r rebound velocity of impacter immediately after initial impact, m/sec (ft/sec)

W width of specimen in test section, m (in.)

ν Poisson's ratio

Subscripts:

x,y Cartesian coordinates. The x-direction corresponds both to the axial direction of the 76.2-cm-diameter (30 in.) full-thickness cylinder and to the hoop direction of the FWC.

ρ,z polar coordinates. The z-direction is normal to the laminate.

MATERIAL

The membrane region of an aft FWC segment was chosen for this investigation. This segment is 3.66 m (12 ft) in diameter, approximately 7.62 m (25 ft) long, and about 36 mm (1.4 in.) thick in the membrane region. The FWC segments are wet-wound by Hercules Inc. using their AS4W-12K graphite fiber and HBRF-55A epoxy resin. From outside to inside, the layup is $(\pm 33.5^\circ)_2/90^\circ/[(\pm\underline{33.5}^\circ)_2/90^\circ]_3/[(\pm 33.5^\circ)_2/90^\circ]_7/(\pm 33.5^\circ/90^\circ_2)_4/(\pm 33.5^\circ)_2/(0^\circ/90^\circ)$, where the 90° layers are the hoops and the $\pm 33.5^\circ$ layers are the helicals. (The 0° direction in the laminate corresponds to the axis of the cylinder.) The number and orientation of the layers was chosen to match the axial stiffnesses of the original steel cases as well as to give adequate strength margins. The underlined $\pm\underline{33.5}^\circ$ helical layers have about 1.6 times as many tows per in. per layer as the other helical layers and are thus thicker in the same proportion. The $0^\circ/90^\circ$ layers at the inner surface are actually one layer of cloth. The layup is balanced (equal numbers of $+33.5^\circ$ and -33.5° layers) but not

symmetrical about the midplane. Most of the hoop layers are closer to the inner surface than the outer surface.

It was not feasible to impact and pressure test full-size FWC segments or to cut specimens from such segments and apply two-to-one biaxial stresses. The most expedient option was to apply uniaxial load to impacted specimens in the most highly stressed direction, which is the hoop direction. Although material was available from prototype FWC's that had been hydrotested, specimens could not have been cut from that material and loaded uniaxially in the hoop direction because the axial load would cause significant bending in the curved specimens. For that reason, a small cylinder was made with full-thickness and winding angles rotated 90° so that the longitudinal direction of the small cylinder was, in effect, the hoop direction of a FWC. Then the specimens could be cut with the loading axis in the longitudinal direction rather than the hoop direction. For unsymmetrical laminates, stretching can cause bending and vice versa. However, for internal pressure type loading, the unsymmetrical laminate does not have bending strains because the FWC is axisymmetric. Also, because the diameter of the FWC is large compared to its thickness, the laminate only has membrane stresses. Therefore, the strains in the laminate due to internal pressure are essentially constant through the thickness. On the other hand, with uniaxial loading, bending strains will develop if the specimen ends are allowed to rotate. However, uniform strains can be produced by using very stiff grips like those used here.

Hercules Inc. had a 76.2-cm-diameter (30 in.), 2.13-meter-long (7 ft) mandrel available, but it could not be used to wind 0° (longitudinal) layers. Thus, unidirectional prepreged broadgoods were hand-laid on the mandrel in lieu of the 0° layers, and the helicals were wound wet. Three plies of the broadgoods were used for each 0° layer to give the same fiber count and thickness as the wet-wound hoop layers in the FWC. From outside to inside, the layup of the small cylinder and hence the specimens was $(\pm 56.5^{\circ})_2/0^{\circ}/[(\pm 56.5^{\circ})_2/0^{\circ}]_3/[(\pm 56.5^{\circ})_2/0^{\circ}]_7/(\pm 56.5^{\circ}/0^{\circ}_2)_4/(\pm 56.5^{\circ})_2/(90^{\circ}/0^{\circ})$. After the cylinder was made, it was cut into seven 30.5-cm-long (12 in.) rings for testing.

The properties of the materials used in making the 76.2-cm-diameter (30 in.) cylinder and the elastic constants of the laminate are given in the Appendix.

TEST APPARATUS AND PROCEDURE

Impact Tests

Two of the rings were impacted by free-falling masses. It was believed that the rings were large enough to simulate the full-sized FWC because the duration of the impacts was short compared to the natural periods of vibration. This was demonstrated in [1] for a thick aluminum beam that was simply supported. Masses were dropped onto the beam at the center of the span for

various span lengths. The impact force decreased with increasing length for lengths up to 30 cm (12 in.) but remained constant for greater lengths. It was also believed that impact force for a FWC containing propellent would be greater than that for an empty FWC because the propellent adds mass and stiffness. Thus, inert propellent was cast in one of the rings by Morton Thiokol International, prime contractor for the FWC, using a procedure similar to that used to cast propellent in an actual FWC. The other ring was left empty.

The free-falling impacters were made of a 5-cm-diameter (2 in.) steel rod with a 1.27-cm-radius (0.5 in.) tup on the end. Four rods of different lengths were used to give masses of 2.8, 5.0, 9.0,and 18.6 kg (6.1, 11.1, 19.9, and 41.1 lbm), including the tup. The corresponding lengths were 16.5, 31.0, 56.6, and 117.6 cm (6.5, 12.2, 22.3, and 46.3 in.). The tup contained a piezoelectric accelerometer and four strain gages for measuring acceleration and impact force. The signals were recorded with an oscilloscope at the rate of 500,000 samples per second. More details about the impacters and their calibration are given in [2].

The filled ring lay on a thin rubber sheet in a shallow aluminum cradle. See figure 1. Its mass, which was 288 kg (635 lbm), was so much greater than that of the impacters that its rebound was imperceptible and attachment to the floor was not necessary. After each impact, the ring was lifted and repositioned with a hoist using the handle that is visible in figure 1. The handle is attached to a rod that passes through a pipe in the center of the propellent. The empty ring lay on the same rubber sheet and cradle during impact. However, its mass was only 40 kg (89 lbm), and it had to be secured to the concrete floor with bolts and a cross-bar to prevent rebound during impact.

Each ring was impacted 44 times with the following masses and kinetic energies.

Mass, kg (lbm)	Kinetic energy, J (ft lbf)	Comments
2.8 (6.1)	41.1 (30.3)	
	82.2 (60.6)	
5.0 (11.1)	37.7 (27.8)	empty ring only
	75.4 (55.5)	
	151. (111.)	
9.0 (19.9)	67.5 (49.8)	
	135. (99.5)	
	270. (199.)	
18.6 (41.1)	69.7 (51.4)	filled ring only
	139. (103.)	empty ring only
	279. (206.)	
	446. (329.)	empty ring only

Prior to impact, 44 impact sites were marked on each ring at equal intervals of arc length of 5.1 cm (2.0 in.) plus an amount to allow for the kerf of the saw and final machining. The impact sites were selected so that no contiguous specimens were impacted with the same mass and energy. Each ring was impacted,

rotated, and impacted again until all 44 impacts were made. The impact damage was localized and never extended into adjacent specimens.

The velocity at a point just above the rings was measured with a laser type velocimeter. Newton's law was used to extrapolate the measured velocity to the surface of the rings. The kinetic energies calculated from the measured velocities were within a few percent of the preselected potential energies of the impacter masses.

The area of contact between the specimen and the 1.27-cm-radius (0.5 in.) impacter was recorded by placing a sheet of paper covered by a sheet of carbon paper on the specimen before the impacter was dropped. The pressure over the contact area transferred carbon to the paper. The diameter of the carbon area was measured with a scale.

Static Compliance Tests

The static compliances of the rings were evaluated for comparison with their dynamic responses. Accordingly, one specimen-site on each ring was not impacted. Instead, the impacter was mounted in a large testing machine and statically pressed against each ring. The force was reacted at the opposite side of the ring, much as in the case of the impact tests. The maximum forces applied to the empty and filled rings were 74.7 and 75.3 kN (16.8 and 16.9 lbf), respectively. These correspond to about 80 percent of the maximum impact forces. The impacter displacement and, for the empty ring, the displacement of the inner surface beneath the impacter were measured. Also, the strengths of these specimens were measured to confirm that strength loss is the same for a statically applied force and an impact force.

X-Ray Tests

After the static compliance tests and impacts were completed, each ring was cut into 44 specimens that were 30.5 cm (12 in.) long and a little wider than 5.1 cm (2.0 in.). The specimens were centered on the impact sites. Next, the cut edges were ground flat and parallel so that the width was 5.1 cm (2.0 in.). Then the impacted face of each specimen was soaked in a zinc iodide penetrant for half an hour, and radiographs were made from the top and side. The penetrant was contained by a circular dam on the surface of the specimen. The depth of impact damage in the radiographs was measured. When the impacters made craters, the surface around the crater was pushed up by the material that was squeezed aside and wedged between layers. Then the depths were measured from the original surface, not the raised surface.

Residual Strength Tests

After the specimens were x-rayed, circular arcs were symmetrically ground into the specimens' edges with a 47.0-cm-diameter (18.5 in.) silicon carbide wheel to reduce the width in the test section to 3.3 or 3.8 cm (1.3 or 1.5 in.). See figure 2. The preliminary investigation in [1] revealed that, even with impact damage, straight sided specimens tended to fail prematurely beneath the leading edges of the grips. The widest test section was desirable in order to

minimize edge effects. Thus, a compromise was made, and the 3.3-cm-wide (1.3 in.) test sections were used for low kinetic energies where the highest strengths were expected, and the 3.8-cm-wide (1.5 in.) test sections for high energies where the lowest strengths were expected. Approximately 8.9 cm (3.5 in.) on each end remained a full 5.1 cm (2.0 in.) wide for gripping.

After the specimens were machined, they were uniaxially loaded to failure in a 445-kN-capacity (100 kips), hydraulic testing machine with hydraulically actuated grips. The grips mostly prevented the specimen ends from rotating. The stroke was controlled because preliminary tests indicated that partial failures were difficult to detect when load was controlled [1]. The load and stroke signals were recorded on an x-y recorder.

To allow for the curved surfaces of the specimens, 9.5-mm-thick (3/8 in.) aluminum shims were placed between the surfaces of the specimens and grips. One surface of each shim was flat and the other was convex or concave to conform to the curvature of the specimens. Sheets of abrasive screen were placed between the shims and specimen to increase the coefficient of friction and prevent slip.

Except for specimens with small impact forces, the impacted specimens failed in two stages as shown in figure 3: first the outer layers with impact damage and then, with increasing load, the undamaged remainder. When the outer layers failed, they also delaminated from the undamaged layers. For each combination of impacter mass and kinetic energy, a duplicate specimen was unloaded when the outer layers failed, removed from the testing machine, and x-rayed. Then, it was reinstalled in the testing machine and loaded to complete failure. Depths of the delaminations in the radiographs were measured.

Strength Tests of Undamaged Specimens

During the course of the investigation, specimens with 2.5-, 3.3- and 3.8-cm-wide (1.0, 1.3, and 1.5 in.) test sections were used. The 2.5-cm-wide (1.0 in.) specimens were used in the preliminary tests but not in the impact tests reported here. In order to increase the data base of undamaged strengths and to determine the effect of specimen width, sixteen undamaged specimens from the other rings were loaded to failure in tension using the same testing machine and procedure as that used for the impacted specimens. The test sections were 2.5, 3.3, and 3.8 cm wide (1.0, 1.3, and 1.5 in.). The strengths were calculated by dividing the loads by the gross area of the test section. The thickness was assumed to be 36 mm (1.4 in.) for all specimens.

As noted previously, pressurization will not cause bending stresses in a FWC even though the laminate is not symmetric. However, uniaxial loading will cause bending if the ends of the specimens are allowed to rotate. The hydraulic grips that were used to load the specimens are relatively stiff and did not allow much rotation. In order to measure the actual bending stress, strain gages were affixed to the inside and outside surfaces of five of the 2.5-cm-wide (1.0 in.) specimens. They were located midway between the edges and ends of the specimens. The results, which are given in [2], revealed that the bending strain was less than seven percent of the membrane strain. With pinned ends, the bending strain was predicted to be as large as 66 percent of the axial strain. Also, some of the undamaged specimens were oriented with the inside surfaces to the front of the testing machine, and others were oriented with the

inside surfaces to the back. The strengths for the two orientations were not significantly different. Thus, the testing machine itself did not induce any bending.

RESULTS AND ANALYSIS

Static Compliance Tests

The displacement of the spherical impacter has two components: overall flexure of the composite ring and local indentation. For a semi-infinite body that is homogeneous and isotropic, the local indentation is given by the Hertz law [3],

$$u_h = \left(\frac{P}{n}\right)^{2/3} \tag{1}$$

where

$$n = \frac{4R_1^{1/2}}{3\pi(k_1 + k_2)}$$

$$k_1 = \frac{1 - \nu_1^2}{\pi E_1}$$

$$k_2 = \frac{1 - \nu_2^2}{\pi E_2}$$

and ν_1, ν_2, E_1, and E_2 are the Poisson's ratio and Young's modulus of the sphere and half-space, respectively, and R_1 is the radius of the sphere.

The flexural component can be represented by a linear spring,

$$u_f = \frac{P}{k_f} \tag{2}$$

where k_f is the spring constant.

Values of k_f and n were calculated from the displacements measured during the static compliance tests. For the empty ring, k_f was calculated from the displacement of the inner surface beneath the impacter, and n was calculated from the displacement of the impacter less the displacement of the inner surface beneath the impacter. The results were $k_f = 5.08$ MN/m (29.0 kips/in.) and $n = 583$ MN/m$^{3/2}$ (531 kips/in.$^{3/2}$). At the maximum force of 74.7 kN (16.8 kips), the flexural displacement given by equation (2) is more than five times the Hertzian indentation given by equation (1). Thus, for static loading, flexure dominates the behavior of the ring.

For the filled ring, the displacement of the impacter was measured, but not that of the inner surface beneath the impacter. The inner surface was inaccessible. Thus, values of k_f and n could not be calculated from the displacements of the filled ring alone. Because the contact stresses decrease rapidly with distance from the contact point and the composite is very thick, the indentations for the filled and empty rings were assumed to be equal. Then k_f was calculated from the impacter displacement less the Hertzian indentation calculated with equation (2) and $n = 583$ MN/m$^{3/2}$ (531 kips/in.$^{3/2}$). The result was $k_f = 6.34$ MN/m (36.2 kips/in.).

The value of k_f for the filled ring is only 25 percent greater than that for the empty ring. Thus, the inert propellent, which has a Young's modulus of 1.2 to 34 MPa (0.18 to 5.0 ksi) depending on loading rate, did not contribute substantially to the static compliance of the ring.

The value of n can also be calculated from the elastic constants of the composite and spherical impacter using equation (1). However, equation (1) was derived for isotropic materials and there is some uncertainty about what to use for E_2. Because most of the deformation is transverse to the laminate, the Young's modulus for the laminae E_{22} is probably a good representation of E_2. Unfortunately, values of E_{22} for the hoop and helical layers were reported to be quite different, 6.39 and 1.92 GPa (0.927 and 0.278 Msi), respectively. (The value for the helical layers was calculated from strains measured on subscale pressure vessels. They may be low because of crazing or premature cracking. The value for the hoop layers was calculated from strains measured on a unidirectional specimen.) Assuming $E_1 = 207$ GPa (30 Msi) for the steel impacter, $\nu_1 = \nu_2 = 0.3$, and $R_1 = 1.27$ cm (0.5 in.), equation (1) gives $n = 1020$ and 313 MN/m$^{3/2}$ (932 and 285 kips/in.$^{3/2}$) for $E_2 = 6.39$ and 1.92 GPa (0.927 and 0.278 Msi), respectively. These values bound $n = 583$ MN/m$^{3/2}$ (531 kips/in.$^{3/2}$). Therefore, E_{22} is a reasonably good estimate for E_2. Conversely, using $n = 583$ MN/m$^{3/2}$ (531 kips/in.$^{3/2}$) and solving equation (1) for an effective value of E_2 gives 3.60 GPa (0.522 Msi).

Impact Tests

Equations (1) and (2) are valid during the impact if the duration of the impact is long compared to the natural periods of vibration. As noted previously, the duration of the impact for the rings is short compared to the natural periods of vibration for the rings. Otherwise, the rings would not represent the FWC. Thus, the value of k_f from the static compliance tests will underestimate the stiffness of the rings during impact as we shall show subsequently. Nevertheless, it will be instructive to use equations (1) and (2) to derive equations for the maximum impact force. The displacement of the impacter is the sum of equations (1) and (2). An equation for the maximum impact force is derived in [3] using the sum of equations (1) and (2) and assuming that energy is conserved. However, the equation is nonlinear and cannot be solved explicitly for the maximum impact force. It will be more convenient here to consider the displacement components separately and to solve explicitly for the maximum impact force. Assuming that the ring is initially stationary and the displacements and forces follow equation (1), one can show by conservation of energy that the maximum impact force is

$$P = n^{2/5}\left[\frac{5KE}{2\left(1 + \frac{m_1}{m_2}\right)}\right]^{3/5} \tag{3}$$

and the impact duration is

$$t_o = 2.942^{-9/10}\left(\frac{5}{n}\right)^{2/5}\left(1 + \frac{m_1}{m_2}\right)^{-2/5} m_1^{1/2}(KE)^{-1/10} \tag{4}$$

where

$$KE = \frac{m_1 v_1^2}{2}$$

is the kinetic energy of the spherical impacter, m_1 and v_1 are the mass and velocity of the impacter immediately before impact, and m_2 is the mass of the composite ring.

Similarly, for the linear flexural spring,

$$P = \left(\frac{2k_f KE}{1 + \frac{m_1}{m_2}}\right)^{1/2} \tag{5}$$

and

$$t_o = \frac{\pi m_1}{k_f\left(1 + \frac{m_1}{m_2}\right)} \tag{6}$$

In equations (3) and (5), maximum impact force increases in proportion to $KE/(1 + m_1/m_2)$ raised to the 3/5 and 1/2 power, respectively. This term will be referred to as the modified kinetic energy, $\bar{K}\bar{E}$. For $m_1/m_2 \ll 1$, $\bar{K}\bar{E} = KE$ and impacter mass has a negligible effect. In equations (4) and (6), the duration of impact increases with increasing impacter mass but varies little (not at all for flexure) with kinetic energy. Therefore, the forms of the equations are very similar for both components of displacement.

Some typical impact force signals are plotted in figures 4 and 5 for the filled and empty rings. Just as predicted by equations (3) - (6), the maximum value of impact force increases with increasing kinetic energy and decreases with increasing impacter mass, and the duration increases with impacter mass but is hardly affected by kinetic energy. Sun and Chen [6] obtained similar results analytically for relatively thin, 1.4 - 2.7 mm (0.05 - 0.11 in.) graphite/epoxy plates impacted with a 12.7-mm-diameter (0.50 in.) steel ball. Although the masses were small, the ratio m_1/m_2 was in the range of those here.

The signals in figures 4 and 5 contain high-frequency oscillations. The intensity of the oscillations increase with increasing kinetic energy, which is equivalent to velocity of the impacter squared v_1^2. Sun and Chen [6] predicted the same type of oscillations in the impact force. They explained that the higher impact velocities excited higher modes of vibration in the plates. However, many of the high frequency oscillations occur at the natural frequencies of the rod-like impacters, indicating that some of the oscillations may be ringing of the impacters.

Notice in figures 4 and 5 that the 9.0 and 18.6 kg (19.9 and 41.1 lbm) impacters collided twice with the empty ring. These two impacters always collided twice with the empty ring, regardless of kinetic energy. The peak value of force for the second impact was less than that for the first impact. These multiple collisions can best be understood by examining the rebound velocities v_r of the impacters in figure 6. The values of v_r were normalized by the corresponding initial velocities v_1 and plotted against the

impacter masses normalized by the ring masses. The masses of the empty and filled rings were 40 and 288 kg (89 and 635 lbm), respectively. The normalized values tend to coincide for the various kinetic energies and the empty and filled rings. The equation

$$\frac{-v_r}{v_1} = 1 - \left(\frac{4m_1}{m_2}\right)^{0.318}$$

fit the data quite well. The two largest values of m_1/m_2 correspond to the 9.0 and 18.6 kg (19.9 and 41.1 lbm) impacters. Notice that these two impacters did not rebound (reverse motion) on the first collision. The 9.0 kg (19.9 lbm) impacter was nearly arrested and the 18.6 kg (41.1 lbm) impacter continued to fall. The empty ring initially moved away from the impacters. However, when the disturbance traveled around the ring and the ring rebounded, the impacters collided a second time with the ring. The less massive impacters rebounded on the first collision and were out of the way when the ring rebounded.

Equations (3) and (5) were derived assuming that the entire mass of each ring acted at a point rather than being distributed around the rings. Thus, an effective mass $\bar{m}_2$ should be used for each ring rather than the total mass m_2. Consider the empty ring to be represented by a spring and mass. Recall that when a moving body collides with a stationary body, the moving body will be arrested if the masses are equal. If the mass of the moving body is less than that of the stationary body, the moving body will rebound or reverse direction and vice versa. Thus, the effective mass $\bar{m}_2$ of a ring corresponds to the mass of the impacter at $v_r = 0$ figure 6. An interpolation of the rebound velocities and masses in gives a value of $m_1/m_2 = 0.25$ for $v_r = 0$. Thus, the effective masses of the rings correspond to one quarter of the static mass, or $\bar{m}_2 = 10.0$ kg (22.0 lbm) and 72.1 kg (159 lbm) for the empty and filled rings, respectively. For the filled ring, all the impacters rebounded. Consequently, $m_1/m_2 = 0.25$ represents an extrapolation of the data in figure 6. Nevertheless, the accuracy of the extrapolation is probably not critical because the difference between $1 + m_1/m_2$ and $1 + m_1/\bar{m}_2$ is only between 3 and 19 percent for the filled ring; whereas, the difference is between 20 and 139 percent for the empty ring.

The maximum values of impact force are plotted against the modified kinetic energy term $KE/(1 + m_1/\bar{m}_2)$ in figure 7 for the filled and empty rings. Because some of the high frequency oscillations might be ringing of the impacter, the maximum impact forces were obtained from the impacter signals after they were smoothed to eliminate the high frequency oscillations. Usually, the peaks of the smoothed and unsmoothed curves differed by less than 1 percent. The data in figure 7 tend to coincide indicating that the dynamic stiffnesses for the filled and empty rings are approximately equal. Thus, the effect of the

inert propellent was to increase the inertia of the composite ring but not the dynamic stiffness. Recall that the static stiffness of the filled ring was only about 25 percent greater than that of the empty ring. The impact forces are very large compared to the weights of the impacters. The accelerations at impact ranged from 277 g's for the 18.6 kg (41.1 lbm) impacter to 2500 g's for the 2.8 kg (6.1 lbm) impacter. Tests of thin composite laminates usually involve kinetic energies and impact forces that are orders of magnitude less than those here.

The symbols were filled in figure 7 to indicate when impacters made visible craters. The craters were visible in the filled ring for impact forces as small as 75.2 kN (16.9 kips) and in the empty ring for impact forces as small as 90.7 kN (20.4 kips). Below the threshold, the impacter only made a slight indentation and gave luster or sheen to the surface -- not a very detectable mark. The transition from crater to no crater was somewhat vague as evidenced by the variability in impact force to cause a crater. The difference between thresholds for the filled and empty rings is probably due to this vagueness or some difference between material properties rather than the presence of the inert propellent.

Equations (3) and (5) with $m_2 = \bar{m}_2$ are also plotted in figure 7 using k_f = 5.08 and 6.34 MN/m (29.0 and 36.2 kips/in.) for the empty and filled rings, respectively. A value of n = 583 MN/m$^{3/2}$ (531 kips/in.$^{3/2}$) was used for both rings. Equation (3) for the Hertz law overestimates the impact forces 6 to 28 percent, depending on $\bar{K}\bar{E}$. However, equation (5) for the flexural spring underestimates the impact forces about 56 percent. Because the total displacement of the impacter during contact is the sum of u_h and u_f in equations (1) and (2), both equations (3) and (5) should overestimate the impact force. (Two springs in series are less stiff than either spring alone.) In order for equation (5) to overestimate impact force, the dynamic value of k_f must be more than four times the static value. Therefore, because of the short duration of the impact, the static stiffness or first mode greatly overestimates the flexural displacements during impact. On the other hand, equation (3) for the Hertz law probably gives a fairly good estimate of the dynamic indentation behavior because of the very local nature of the indentation.

Viscoelasticity of the epoxy matrix could also cause the dynamic value of k_f to be underestimated. However, n should also have been affected, and yet it overestimated the impact force as it should. Thus, viscoelasticity was probably not a significant factor.

Because u_h and u_f in equations (3) and (5) are both proportional to $\bar{K}\bar{E}$ raised to the 3/5 and 1/2 powers, respectively, the actual impact force is approximately proportional to $\bar{K}\bar{E}$ raised to a power between 3/5 and 1/2. The equation

$$P = C_1 \left(\frac{KE}{1 + \frac{m_1}{m_2}} \right)^{0.516} \qquad (7)$$

with $C_1 = 6860\ N^{0.484}\ m^{-0.516}$ ($1810\ lbf^{0.484}\ ft^{-0.516}$) fits the data without craters in figure 7 quite well. The value of C_1 and the exponent 0.516 were determined by a linear regression analysis. When craters were made, the impact forces were smaller than those given by equation (7), indicating that the damage had a softening effect.

Strengths

Undamaged specimens.- The undamaged strengths were not significantly affected by specimen width. The average strength for 19 specimens is 345 MPa (50.1 ksi) and the coefficient of variation is 0.0805.

Hercules Inc. made and tested numerous quarter-scale cylinders 91.4 cm (36 in.) in diameter to determine design allowables for the FWC. The mean strength, in terms of hoop-fiber stress, for the tensile specimens is 38 percent less than that for the cylinders, 2.19 GPa (317 ksi) compared to 3.54 GPa (544 ksi). The mean strength of the fibers in the quarter scale cylinders, as determined from fiber-lot-acceptance tests, was 4.07 GPa (590 ksi) [1] and that of the broadgoods fiber in the 76.2-cm-diameter (30 in.) cylinder with full thickness was 3.75 GPa (544 ksi). Thus, one would expect the stress in the hoop fibers of the tensile specimens at failure to be about 3.54x3.75/4.07 = 3.26 GPa (473 ksi), not 2.19 GPa (317 ksi)!

On the basis of lamination theory, the helical layers only carry 20 percent of the axial load. Thus, had edge effects prevented the helical layers from carrying any load, the strengths would have been reduced only 20 percent, not 33 percent. Helical layers on the surfaces sometimes failed at the grips, but the interior layers failed in the test section. Thus, neither edge effects nor grip failures could have caused the low strengths.

Photographs of an edge of a tensile coupon and a coupon cut from the excess material at the end of an actual FWC case are shown in figure 8. Although the layups are different, notice that the hoop layers (light bands) of the FWC case are straight, but those of the tensile specimen are wavy. The inset shows an enlargement of one wrinkle that is so high the epoxy did not fill in beneath it. These wrinkles are part of a pattern of waviness that occurs throughout all the specimens in varying degrees. It was probably caused when the helical layers were wound over the hand-layed hoop layers, which had no pre-tension.

For carbon/carbon composites, Jones and Studdert [7] noted that wrinkle-free laminates are stronger than wrinkled laminates. The differences in strength were not given. However, in experiments conducted by of one of the present authors (Poe), two 16-ply-panels made of graphite/epoxy tape failed at remote wrinkles rather than at 13-cm-long (5 in.) cuts at the center of the panels. The strengths were about half those of an uncut laminate, indicating

that the stress concentration factor at the wrinkles was about two. In the tensile specimens here, a stress concentration factor of only 1.6 would account for a 33 percent loss in strength. Thus, the wrinkles in the hoop layers probably caused the low strengths.

Impacted specimens.- As shown previously in figure 3, except for small impact forces, specimens failed in two stages: first the outer layers containing the impact damage and then, with increasing load, the remainder. When the outer layers failed, they also delaminated from the undamaged layers. These failures will be referred to as first- and remaining-ligament failures, respectively. For small impact forces, the laminate did not fail in two stages; instead, all layers failed simultaneously. Radiographs of two impacted specimens made before and after loading to first-ligament failure are shown in figures 9(a) and 9(b). Both specimens came from the filled ring, but they are representative of specimens from both rings. The impact forces for specimen 7-7 and 7-8 were 60.0 and 79.2 kN (13.5 and 17.8 kips), respectively. The impact damage caused a visible crater in specimen 7-8, but not in specimen 7-7. A top and a side view are shown in figure 9 for each load condition. In the side views, the dark narrow bands are the hoop layers and the light bands are the helical layers. The delaminations in the radiographs made after loading to first-ligament failure are not confined to a single interface or plane but meander among layer interfaces. Thus, the delaminations do not appear as narrow lines in the radiographs of the sides but as wide dark bands. The innermost path of the delaminations seem to lie at interfaces of hoop and helical layers. It is important for the reader to understand that these delaminations were caused by the loading, not the impacts. The impacts themselves did not cause delaminations.

Specimens with semi-elliptic surface cuts failed similarly with the cuts acting like impact damage [1,8]. For very shallow cuts, the laminate failed as one part, much like a metal. The stress at which the top part failed decreased with increasing cut size according to linear elastic fracture mechanics, and the strength of the bottom part varied inversely with its thickness, much as an uncut laminate. Similar results were reported in [9] for a 10-mm-thick (0.4 in.) quasi-isotropic T300/5208 laminate.

The stresses to fail the first and remaining ligaments were divided by the mean undamaged strength of 345 MPa (50.1 ksi) and plotted in figures 10(a) and 10(b), respectively. Stresses were calculated by dividing the loads by the gross area of the test section, just as they were for the undamaged strengths. When the impact forces were small and the specimens failed in one stage, the strengths were plotted in both figures. Therefore, the failing stresses in figure 10(b) are also the ultimate strengths of all the specimens. Different symbols were used for the empty and filled rings, and the symbols were filled when the impacters made craters. The impact force threshold for visible damage is indicated by the vertical line at 75.2 kN (16.9 kips). The stresses for first-ligament failure decrease with increasing impact force. On the other hand, the stresses for remaining-ligament failure appear to be more independent of impact force, even when the impacters made craters. For the largest impact forces, the stresses for first-ligament failure are as low as 50 percent of the mean undamaged strength. On the other hand, the stresses for remaining-ligament failure are no lower than 75 percent of the mean undamaged strength. At the

threshold for visible damage, the lowest stresses for first- and remaining-ligament failures are 63 and 78 percent of the mean undamaged strength, respectively.

The individual undamaged strengths were also plotted in figures 10(a) and 10(b) for comparison. The failing stresses of the impacted and undamaged specimens overlap considerably. For several specimens, in fact, the stress to fail the remaining ligament is greater than the mean undamaged strength. Nevertheless, the coefficients of variation among specimens with the same impact conditions is not large [2]. It is typically less than 0.1. Also, the failing stresses for specimens from the filled ring are typically 5 to 10 percent higher than those for specimens from the empty ring. It is believed that this difference is caused by material or testing variations and not by the inert propellant.

The failing stresses for the two specimens that were statically "impacted" in the static compliance tests were also plotted in figures 10(a) and 10(b). They fall among the impacted strengths indicating that the static and impact tests were equivalent.

The fracture toughness and undamaged strengths were reduced by the wrinkles in the same proportion [1]. Consequently, the ratios of strengths with and without surface cuts were not affected by the wrinkles. Because the behavior of specimens with impact damage and surface cuts was similar, it is believed that the strength ratios in figure 10 can be applied directly to the FWC despite the wrinkles.

It is not known if the uniaxial strengths in figures 10(a) and 10(b) are greater or less than strengths in a biaxial stress field like that in a cylindrical pressure vessel. For thin graphite/epoxy laminates with holes, Daniel [10,11] obtained mixed results. For one layup and stress ratio, the uniaxial strengths were 20 percent greater than the biaxial strengths; and, for another layup and stress ratio, they were 20 percent less than the biaxial strengths.

When the specimens failed in two stages, the remaining-ligament strengths were usually larger than the first-ligament strengths. Thus, the two-part failures constituted redundancy or fail-safeness in some measure. However, the delamination that accompanied the first-ligament failure spread throughout the tensile specimens and could itself constitute structural failure. Then the two-part failure would not be fail-safe.

Hercules, Inc. hydrotested four quarter-scale cases with impact damage. The cases did not appear to fail as two parts like the tensile specimens. By using fracture mechanics, it was shown in [2] that two-part failure will not occur in the thin laminate of the quarter-scale cases with hydrostatic pressure. Also, for a given depth of damage, the strengths may be less in the thin laminate than the thick laminate. Thus, impact damage is very difficult to represent in subscale pressure vessels.

Impact Damage

Predictions and radiographs.- Love's solution for stresses in a semi-infinite body produced by hemispherical pressure on part of the boundary [12] was used to predict the depth of impact damage in terms of impact force. The body is assumed to be homogeneous and isotropic. Even so, the results should be accurate, at least qualitatively, when the contact diameter is large compared to layer thickness.

Love's solution gives no tension stresses beneath the contact area. On the other hand, the compression stress in the plane of the fibers is as large as $(1/2 + \nu_2)p_c$, where p_c is the average contact pressure at the center of the contact surface. However, as will be shown subsequently, the observed mode of fiber failure did not appear to be shear kinking or micro-buckling, which is usually associated with compression failures. Therefore, a maximum shear criterion was assumed for failure of the fibers. Principal shear stress contours from Love's solution are plotted in figure 11 for various ratios of average contact pressure to shear strength. These stress contours are equivalent to damage contours. The coordinates z and ρ are normalized by the contact radius. The average contact pressure p_c is the impact force divided by the contact area or $p_c = P/(\pi D^2/4)$. The maximum value of the hemispherical pressure is 1.5 times the average value and occurs at $\rho = 0$. The contours in figure 11 are approximately circular in cross section, giving a somewhat spherical damage region.

The maximum and minimum depths of the damage contours ($\rho = 0$) are plotted against the contact pressure in figure 12. The damaged envelope is cross-hatched. Damage initiates below the surface at $2z/D = 0.47$ when the contact pressure is approximately 1.61 times the shear strength. As the pressure increases, the damage spreads up and down and reaches the surface at a pressure equal to approximately 5.0 times the shear strength.

In order to use the curve in figure 12 to predict the depth of impact damage, the shear strength, the contact radius, and the contact pressure must be known. The contact diameter measured with the carbon paper is plotted against impact force in figure 13. Different symbols were used to indicate when the impacters made craters. (In the empty ring, the contact area was inadvertently not measured for the largest kinetic energy when the impacters made craters.) The paper was obliterated in the contact area when the impacters made craters, and the outline of the area was somewhat ragged. Thus, the dispersion is greater when impacters made craters. For the Hertz law [3], the contact diameter is

$$D = 2R_1^{1/2}\left(\frac{P}{n}\right)^{1/3} \tag{8}$$

A regression analysis of the data without permanent craters using equation (8) gave $n = 448$ MN/m$^{3/2}$ (408 kips/in.$^{3/2}$). Equation (8) models the contact diameters in figure 13 very well except when the impacters made craters. Then,

the contact diameters were considerably greater than equation (8) predicted. Recall that the indentation depth in the static compliance test was modeled by equation (1) with a value of $n = 583$ MN/m$^{3/2}$ (531 kips/in.$^{3/2}$), reasonably close to 448 MN/m$^{3/2}$ (408 kips/in.$^{3/2}$). Thus, the Hertz law models the indentation depth and contact diameter fairly accurately for both static loads and impact.

The impact forces divided by the circular contact area $\pi D^2/4$ are plotted against impact force in figure 14. Different symbols were used when impacters made craters. Without craters, the pressures are 480 to 690 MPa (70 to 100 ksi). (Recall that the peak value of the hemispherical pressure in Love's solution is 50 percent greater than the values in figure 14.) When craters were made, the contact diameters increased so much that the pressures dropped about 40 percent. Eliminating the contact diameter in equation (8) with $D = [4P/(\pi p_c)]^{1/2}$ and solving for the average contact pressure p_c,

$$p_c = \left(\frac{n}{\pi R_1}\right)\left(\frac{P}{n}\right)^{1/3} \tag{9}$$

Equation (9) with $n = 448$ MN/m$^{3/2}$ (408 kips/in.$^{3/2}$) is also plotted in figure 14. The calculated pressures and equation (9) agree likewise. Notice that both contact diameter and pressure increase in proportion to impact force to the 1/3 power.

The only remaining information that is needed to predict damage depth is the shear strength S_u. Two values were used, one for the matrix and another for the fibers. A value of $S_u = 103$ MPa (15 ksi), which is typical for the shear strength of unidirectional graphite/epoxy, was used for the matrix, and a value of $S_u = 310$ MPa (45 ksi) was used for the fibers. The value for the fibers was obtained by compressing disks that were cut from several specimens using core drills. See figure 15. Compression loads were applied to both faces of each disk, giving loading on the outer surface similar to the impact loading. The diameters of the disks were 2.5, 3.8, and 5.1 cm (1.0, 1.5, and 2.0 in.). Several specimens with each diameter were crushed. The average compression strength was 620 MPa (90 ksi). The strength varied little with specimen diameter. The failure surfaces intersected the free edge at a 45° angle, typical of shear. The shear stress at the free edge is 1/2 the compression stress. It may be slightly greater in the interior. Thus, the shear strength is approximately 310 MPa (45 ksi).

Using equations (8) and (9) and the curve for damage depth in figure 12, the depth of damage was calculated and plotted in figure 16 for the values of $S_u = 103$ and 310 MPa (15 and 45 ksi). The locations of hoop layers are indicated on the ordinate. The minimum values of impact force for the curves in figure 16 are 1.1 and 29.7 kN (0.25 and 6.68 kips) for $S_u = 103$ and 310 MPa (15

and 45 ksi), respectively. They represent the thresholds for matrix and fiber damage and increase in proportion to S_u to the third power. (This was incorrectly reported in [2] as the one-third power.) The matrix damage initiates in the outer helical layers, about one-third of the distance to the first hoop layer and reaches the surface for impact forces greater than 33.5 kN (7.53 kips). On the other hand, the fiber damage initiates in the first hoop layer and reaches the surface for impact forces greater than 907 kN (204 kips). The depth at which the damage initiates increases in proportion to the shear strength.

The depths of impact damage revealed in the radiographs are also plotted in figure 16. Filled symbols were used to indicate when the impacters made craters. The depths are very similar in the filled and empty rings for the same impact force. The damage was not evident in the radiographs for impact forces less than 40 kN (9 kips). The damage was not always evident for impact forces between 40 (9 kips) and 89 kN (20 kips). However, it was always evident when impacters made craters. In general, damage depth in the radiographs increased with impact force above 40 kN (9 kips) and did not extend below the second hoop layer.

If the dye penetrated to the innermost matrix damage, the depth of damage in the radiographs should correspond to the predicted curve for matrix damage. However, it does not; the depths in the radiographs correspond more to the predicted curve for fiber damage. Actually they are a little less than the curve for fiber damage. Radiographs were made of a specimen with an impact force of 81.4 kN (18 kips) before and after a small hole was drilled deep into the impact site [1]. There was no visible surface damage. The radiograph made before the hole was drilled also did not reveal damage. However, the radiograph made afterward did. Therefore, the dye apparently has difficulty penetrating the damage. Also, the damage depths are probably overpredicted somewhat because isotropic theory gives larger stresses than anisotropic theory [3]. On the other hand, the impact force threshold for appearance of damage in the radiographs does agree fairly well with the force at which the predicted matrix damage reaches the surface. However, the force threshold for causing craters, which is about 75.2 kN (16.9 kips), is an order of magnitude less than 907 kN (204 kips) that is predicted for the fiber damage to reach the surface.

Equivalent cut depths.- The failure modes of specimens with surface cuts were the same as those with impact damage, indicating that depths of impact damage and surface cuts are equal for equal remaining-ligament strengths. Thus, depths of impact damage can be inferred from remaining-ligament strengths and surface cut data. These depths will be referred to as equivalent cut depths to distinguish them from other measurements or predictions of impact damage depth. They were calculated with the following equation, which was fit to the remaining-ligament strengths of specimens with surface cuts [1].

$$a = \left(\frac{C_2}{S_c}\right)^{3.60} \tag{10}$$

where C_2 = 0.208 MPa $m^{1/3.6}$ (30.1 ksi $in.^{1/3.6}$) and S_c is the remaining-ligament strength. The equivalent surface cut depths, which were calculated only for specimens that failed as two parts, are plotted against impact force in figure 17. The filled and empty symbols represent the filled and empty rings, respectively. The large exponent in equation (10) would greatly amplify the scatter in strengths among like specimens. Thus, the average values for a given impacter mass and kinetic energy, rather than individual values, were plotted to clarify the trends. The location of the hoop layers are shown on the ordinate. Also, the depths of matrix and fiber damage predicted with shear strengths of 103 and 310 MPa (15 and 45 ksi), respectively, were plotted for comparison. The equivalent cut depths are between those predicted for fiber and matrix failure but agree best with the fiber-failure curve for large impact forces. The values of equivalent cut depth were smaller for the filled ring than the empty ring because the filled ring was 5 to 10 percent stronger than the empty ring.

The average depths of impact damage in the radiographs made before loading are also plotted in figure 17 for comparison. For small impact forces, the damage depths in the radiographs are much less than the equivalent cut depths. But, for large enough impact forces to cause craters, the damage depths are more nearly equal to the equivalent cut depths. Therefore, the radiographs reveal much less impact damage than that implied by the remaining-ligament strengths when there is no surface damage. Although the values of equivalent cut depth were smaller for the filled ring than the empty ring, the damage depths in the radiographs were not.

Delamination depths after loading to first-ligament failure.- For 80 ply quasi-isotropic T300/5208 laminates with surface cuts, the delamination that accompanied first-ligament failure developed at the bottom of the cut [9]. However, for surface cuts in the FWC laminate [8], the delamination was not always at the bottom (private communication from Dr. D. H. Morris, Virginia Polytechnic Institute and State University, Blacksburg, Virginia). It was at the interface of hoop and helical layers that was nearest the bottom of the surface cut. For this reason, the delamination depths could differ from the surface cut depths by as much as half the thickness of a group of helical layers, which is 1.4 mm (0.055 in.) for the $(\pm 56.5)_2$ double helical layers near the outer surface. In the T300/5208 laminate, the delamination could also have been at the interface of the $\pm 45^\circ$ and 0° layers nearest the bottom of the surface cut. However, the difference probably would not have been noticed because only about 0.4 mm (0.016in.) separates the 0° plies.

The depths of delaminations in the radiographs were measured and plotted against impact force in figure 18. Average values of equivalent cut depths were also plotted for comparison. (The delamination depths are not averages.) The filled symbols represent the filled ring and the empty symbols represent the empty ring. If impact damage is equivalent to a surface cut, one would expect the delamination depths to be deeper than the equivalent cut depths by no more than half the thickness of a group of helical layers. This was true for specimens from the empty ring, indicating that the delamination and equivalent cut depths were consistent. For specimens from the filled ring, the delamination depths were a full thickness of helical layers below the equivalent cut depths. As noted previously, the specimens from the filled ring were 5 to

10 percent stronger than those from the empty ring, and the equivalent cut depths were correspondingly less. Because the damage depths in the radiographs were equal for the filled and empty rings and the delamination depths were equal for the filled and empty rings, the difference between strengths of the filled and empty rings is probably due to material variation or load measurement error rather than impact damage. Nevertheless, the equivalent cut depths and the delamination depths both indicate that the radiographs made before loading do not reveal the full extent of impact damage, even when the impacts caused craters.

Actual impact damage to the fibers was also determined by destructively examining a specimen after impact. This specimen was not from the two intact rings. Instead, it was cut from another ring and then impacted while lying on inert propellent. The impact force was 54.3 kN (12.2 kips). A 2.5-cm by 2.5-cm (1-in. by 1-in.) coupon of full thickness was cut from the impact site, and the layers were separated by heating to a temperature of 422 °K (350 °F) and holding for 90 minutes). Then, the individual layers were examined with an optical microscope and a scanning electron microscope for broken fibers. The layers from the surface through the second helical layer below the first hoop layer, inclusively, contained obviously broken fibers. Two photographs of the deepest layer with damage, which was 3.6 mm (0.14 in.) from the surface, are shown in figure 19. They were made in the scanning electron microscope with 13X and 280X magnification. A 5.1-mm-long (0.20 in.) "crack" (locus of fiber breaks) can be seen in the 13X photograph. The "crack" was directly below the impact site and oriented normal to the fibers. The "cracks" in layers above this layer were similar, and all the layers below this layer were largely free of "cracks." The "cracks" in each layer were oriented normal to the fibers. The region of the "crack" covered by the 280X photograph is outlined by the rectangle drawn on the 13X photograph. The individual fiber breaks can be seen in the 280X photograph. The broken fibers do not have the appearance of fibers that have failed in compression by shear kinking or micro buckling.

The depth of the "cracked" layer in figure 19 was also plotted in figure 18 for the corresponding impact force and labeled "deply". It is less than the equivalent surface cuts and delaminations. However, it is almost as deep as the predicted curve for 310 MPa (45 ksi), which corresponds to fiber failure. Perhaps fibers below the "cracked" layer in figure 19 were weakened but not visibly broken in the deplied layers, causing lower remaining-ligament strengths. Elber [4] found evidence to this effect. He removed fiber bundles from the impact site of a thin graphite/epoxy laminate and loaded them to failure. The strengths of some bundles were 30 to 50 percent of the undamaged strength without a corresponding number of visibly broken fibers (private communication from Dr. Elber, U.S. Army Aerostructures Directorate, USAARTA - AVSCOM, Langley Research Center, Hampton, Virginia).

The predicted curves for shear strengths of 103 and 310 MPa (15 and 45 ksi) in figure 18 represented matrix and fiber failure, respectively. An intermediate strength can be associated with fibers that are weakened but not broken. Accordingly, a curve was predicted and plotted in figure 18 for a strength of 241 MPa (35 ksi). This curve, which passes through the approximate median of the equivalent cut depths and impact forces, indicates the sensitivity of damage depth to shear strength.

CONCLUSIONS

A special 76.2-cm-diameter (30 in.) cylinder, 36-mm (1.4 in.) thick, was made to represent the membrane of a graphite/epoxy solid rocket motor for the space shuttle. Two 30.5-cm-long (12 in.) rings were cut from the cylinder and impacted with 1.27-cm-radius (0.50 in.) impacters. One of the rings was filled with inert propellent and one was empty. The masses of the impacters varied from 2.8 to 18.6 kg (6.1 to 41.1 lbm) and the kinetic energies from 37.7 to 446 J (30.3 to 329 ft lbf). Specimens with a width of 5.1 cm (2.0 in.) were cut out of the two rings and uniaxially loaded to failure in tension to determine the strength loss due to the impacts. Specimens were x-rayed and ultrasonically scanned to determine the amount of impact damage. Also, one specimen was destructively examined (deplied by pyrolysis) to determine the extent of actual broken fibers. The strengths and depths of impact damage were analyzed in terms of maximum impact force. Rigid body mechanics and the Hertz law were used to derive an equation for impact force in terms of kinetic energy and the masses of the impacters and rings. The depth of damage was predicted in terms of impact force using Love's solution for pressure applied on part of the boundary of a semi-infinite body. The results indicate the following:

1. Impact force increased in proportion to $KE/(1 + m_1/\bar{m}_2)$ raised to the 0.516 power, where KE and m_1 are the kinetic energy and mass of the impacter, respectively, and $\bar{m}_2$ is 1/4 the total mass of the filled or empty ring.

2. The stiffnesses of the filled and empty rings were nearly equal. However, the apparent flexural stiffnesses during impact were more than four times the static values.

3. The impacted specimens failed as two parts when loaded, much like specimens with surface cuts. Except for very shallow damage, the damaged outermost layers failed first; and then, with additional load, the remaining or undamaged part. The first part delaminated from the remainder when it failed. For very shallow damage, the specimens failed as one part, much like a metal. The stresses at which the two parts failed decreased with increasing impact force, more for the first part than the remainder. For the largest impact forces, the stresses to fail the first and remaining parts were as low as 50 and 75 percent of the mean undamaged strengths, respectively.

4. Impact forces ranged from 36 to 98 kN (8 to 22 kips). For impact forces less than 75.2 kN (16.9 kips) damage was not visible. Above 75.2 kN (16.9 kips), the impacts usually caused visible surface craters. Conventional ultrasonic attenuation maps revealed no damage. The radiographs did not reveal damage for impact forces below 40 kN (9 kips). They sometimes revealed damage for impact forces above 40 kN (9 kips) and always revealed damage when the impacts caused craters. However, the radiographs never revealed the full depth of damage. Impact damage inferred from remaining-ligament strengths and delaminations was considerably deeper, especially for the smallest

impact forces. The predicted threshold for causing fiber damage was about 30 kN (6.7 kips). For nonvisible damage, the stresses to fail the first and remaining ligaments were as low as 63 and 78 percent of the mean undamaged strengths, respectively.

5. The undamaged strength was about 39 percent less than expected on the basis of fiber-lot-acceptance tests. Wrinkles in the 0° layers probably caused the low strengths. It is believed that the wrinkles reduced the strengths of the impacted specimens likewise. For this reason, the ratios of impact strength to undamaged strength should not have been affected by the wrinkles.

6. The Hertz law gave reasonably correct local deformations, contact diameters, and contact pressures except when craters were made.

7. The depth of broken fibers was reasonably well predicted using Love's solution for pressure applied on part of the boundary of a semi-infinite body and a principal shear stress criterion.

APPENDIX - MATERIAL PROPERTIES

The graphite fiber is Hercules Inc.'s AS4W-12K, and the winding resin is Hercules Inc.'s HBRF-55A. The epoxy in the unidirectional broadgoods is Hercules Inc.'s MX-16. Fiber-lot-acceptance (FLA) tests were conducted on the fiber used to make the test case. Properties of the helical fiber, broadgoods fiber, and matrix or winding resin are given in the table below. (The helical and broadgoods fibers were from different lots.)

	Helical fiber	Broadgoods fiber	Matrix
Tensile modulus, GPa (Msi) ...	228 (33)	228 (33)	2.85 (0.414)
Poisson's ratio	-	-	.35
Tensile strength, GPa (ksi) ..	3.96 (574)	.75 (544)	-
Elongation at failure	0.0167	-	-
Density, kg/m^3 ($lbm/in.^3$)	1790 (0.0648)	1780 (0.0642)	1230

Physical properties and lamina constants were measured by Hercules Inc. on six coupons cut from the ends of the test case. The physical properties are

Composite density, kg/m^3 ($lbm/in.^3$) ..	1490 (0.05397)
Resin mass fraction	0.3459
Resin volume fraction	0.3845
Fiber volume fraction	0.5449
Void content	0.0706

and the lamina constants are

	Unidirectional broadgoods	Helical layers	Cut helical layers	Cloth
E_{11}, GPa (Msi)	1.06	111	111	59.3
	(15.4)	(16.2)	(16.2)	(8.60)
E_{22}, GPa (Msi)	6.39	1.92	1.92	59.3
	(0.927)	(0.278)	(0.278)	(8.60)
G_{12}, GPa (Msi)	4.47	4.28	4.28	3.68
	(0.649)	(0.621)	(0.533)	(0.533)
ν_{12}	0.275	0.267	0.267	0.0348
Thickness per ..... layer, mm (in.)	[a]0.427	0.427	0.711	0.427
	(0.0168)	(0.0168)	(0.0280)	(0.0168)

[a]Equal to three plies of broadgoods.

The elastic constants of the test case laminate were predicted with lamination theory using the lamina constants in the table above. It was assumed that bending and stretching were not coupled, that is, the laminate was symmetric. The predictions are E_x = 30.6 GPa (4.44 Msi), E_y = 39.0 GPa (5.66 Msi), G_{xy} = 19.7 GPa (2.86 Msi), ν_{xy} = 0.351, and ν_{yx} = 0.447. (The x-direction corresponds to the axial direction of the test case and the hoop direction of the FWC.)

REFERENCES

1. Poe, Jr., C. C.; Illg, W.; and Garber, D. P.: A Program to Determine the Effect of Low-velocity Impacts on the Strength of the Filament-wound Rocket Motor Case for the Space Shuttle. NASA TM-87588, September 1985.

2. Poe, Jr., C. C.; Illg, W.; and Garber, D. P.: Tension Strength of a Thick Graphite/epoxy Laminate after Impact by a 1/2-In.-Radius Impacter. NASA TM-87771, July 1986.

3. Greszczuk, Longin B.: Damage in Composite Materials due to Low Velocity Impact. Impact Dynamics, John Wiley & Sons, Inc., 1982, pp. 55-94.

4. Elber, Wolf: Failure Mechanics in Low-Velocity Impacts on Thin Composite Plates. NASA TP-2152, May 1983.

5. Shivakumar, K. N.; Elber, W.; and Illg, W.: Prediction of Impact Force and Duration During Low Velocity Impact on Circular Composite Laminates. Journal of Applied Mechanics, vol. 52, September 1985. pp. 675-680.

6. Sun, C. T.; and Chen, J. K.: On the Impact of Initially Stressed Composite Laminates. Journal of Composite Materials, vol. 19, Nov. 1985, pp. 490-504.

7. Jones, Walter C.; and Studdert, G. Michael: Improved Processing Developments for Carbon/Carbon Composites. Society of Aerospace Material and Process Engineers. Proceedings of 16th National Symposium and Exhibit, vol. 16, April 1971. pp. 67-80.

8. Harris, C. E.; and Morris, D. H.: Preliminary Report on Tests of Tensile Specimens with a Part-Through Surface Notch for a Filament-Wound Graphite/Epoxy Material. NASA CR-172545, 1985.

9. Harris, C. E.; and Morris, D. H.: The Fracture of Thick Graphite/Epoxy Laminates with Part-Through Surface Flaws. Composite Materials: Fatigue and Fracture, ASTM STP 907, American Society for Testing and Materials, 1986, pp. 100-114.

10. Daniel, Issac M.: Behavior of Graphite/Epoxy Plates with Holes under Biaxial Loading. Experimental Mechanics, vol. 20, 1980, pp. 1-8.

11. Daniel, Issac M.: Biaxial Testing of $[0_2/\pm 45]_s$ Graphite/Epoxy Plates with Holes. Experimental Mechanics, vol. 22, 1982, pp. 188-195.

12. Love, A. E. H.: The Stress Produced in a Semi-infinite Solid by Pressure on Part of the Boundary. Phil. Trans. Roy. Soc. Lond. Series A, vol. 228, 1929, pp. 377-420

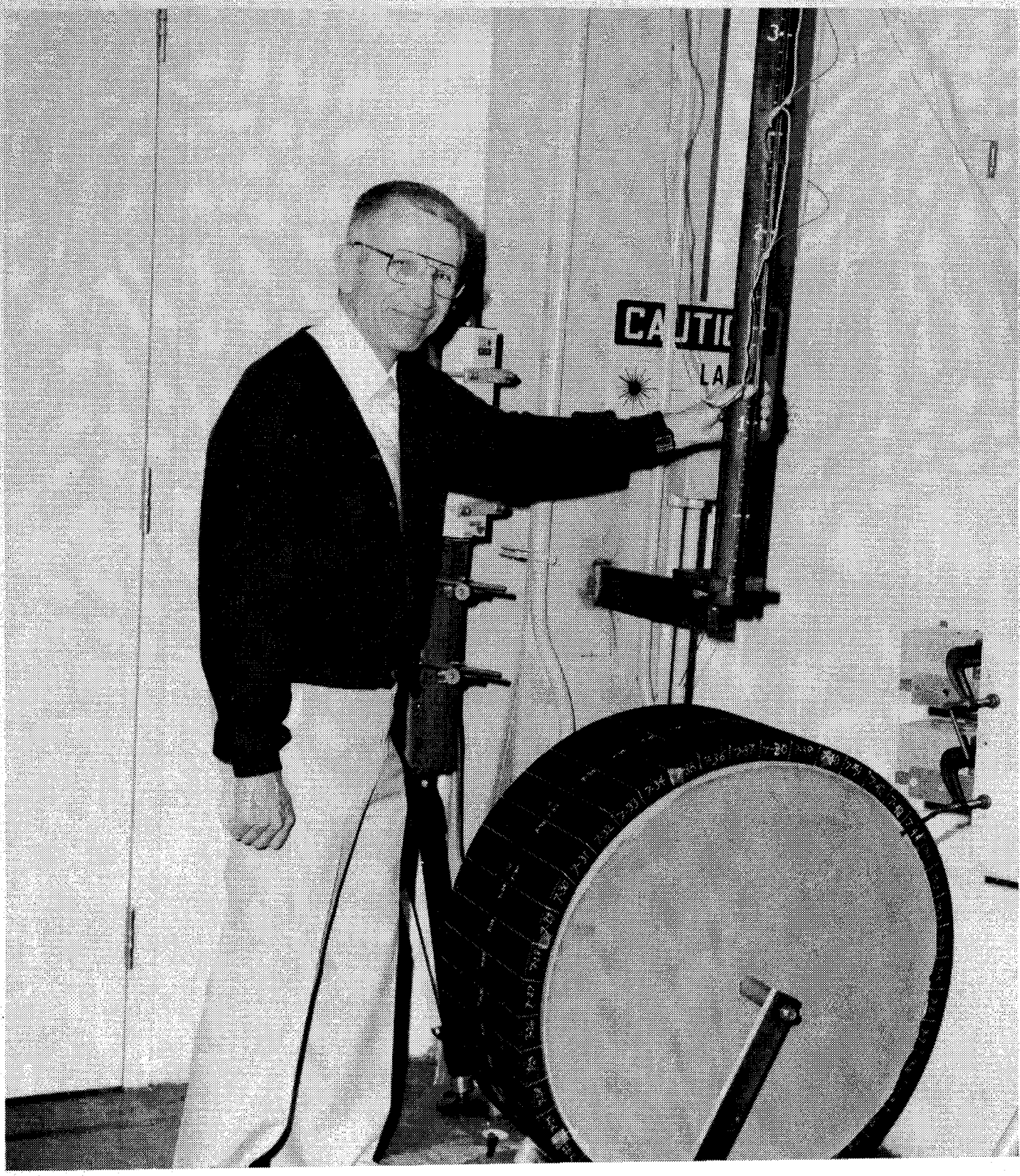

NASA
L-85-5491

Figure 1.- Photograph of filled ring and part of the impact apparatus.

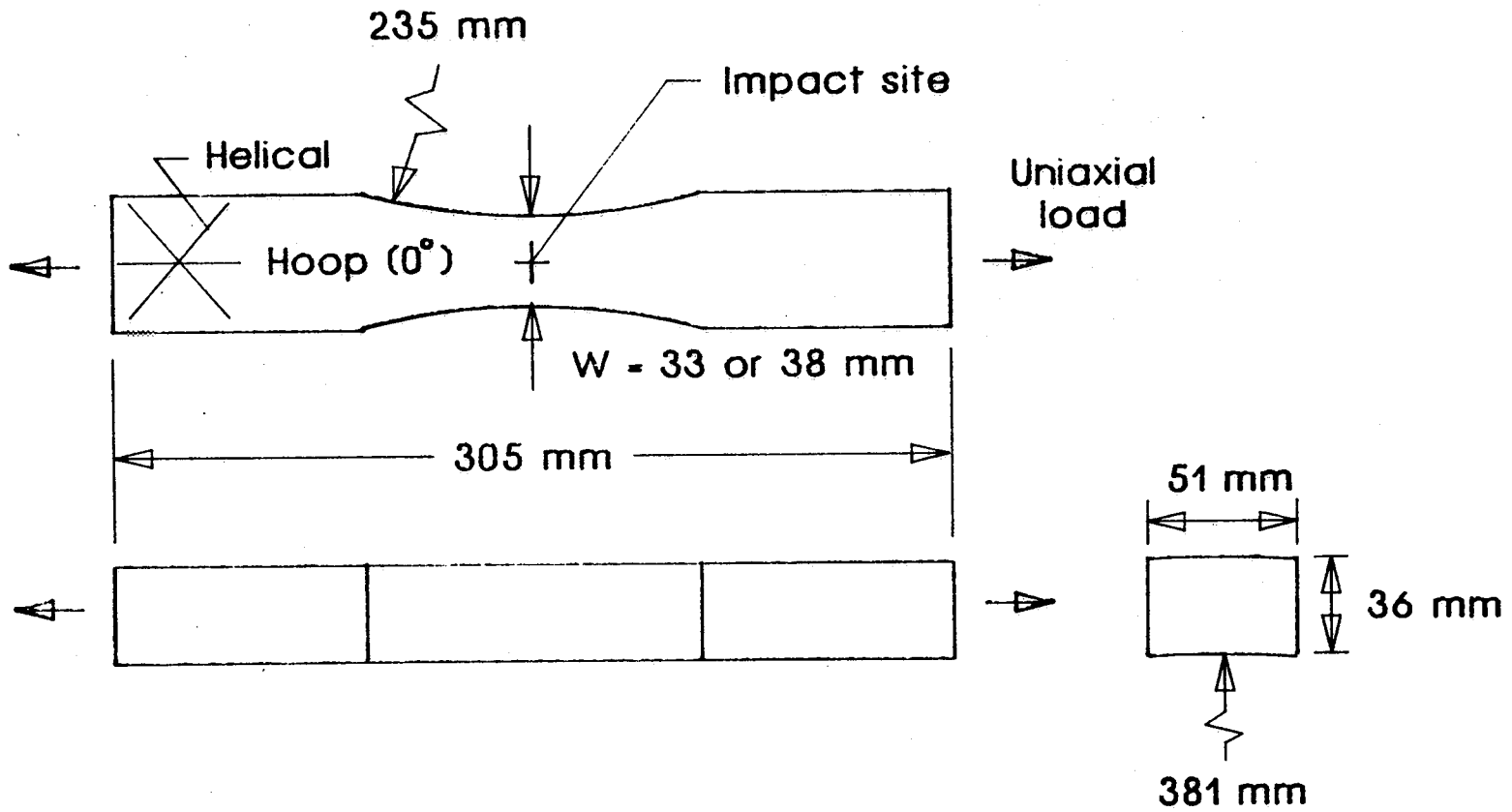

Figure 2.- Sketch of tensile specimen.

FIG2.AST

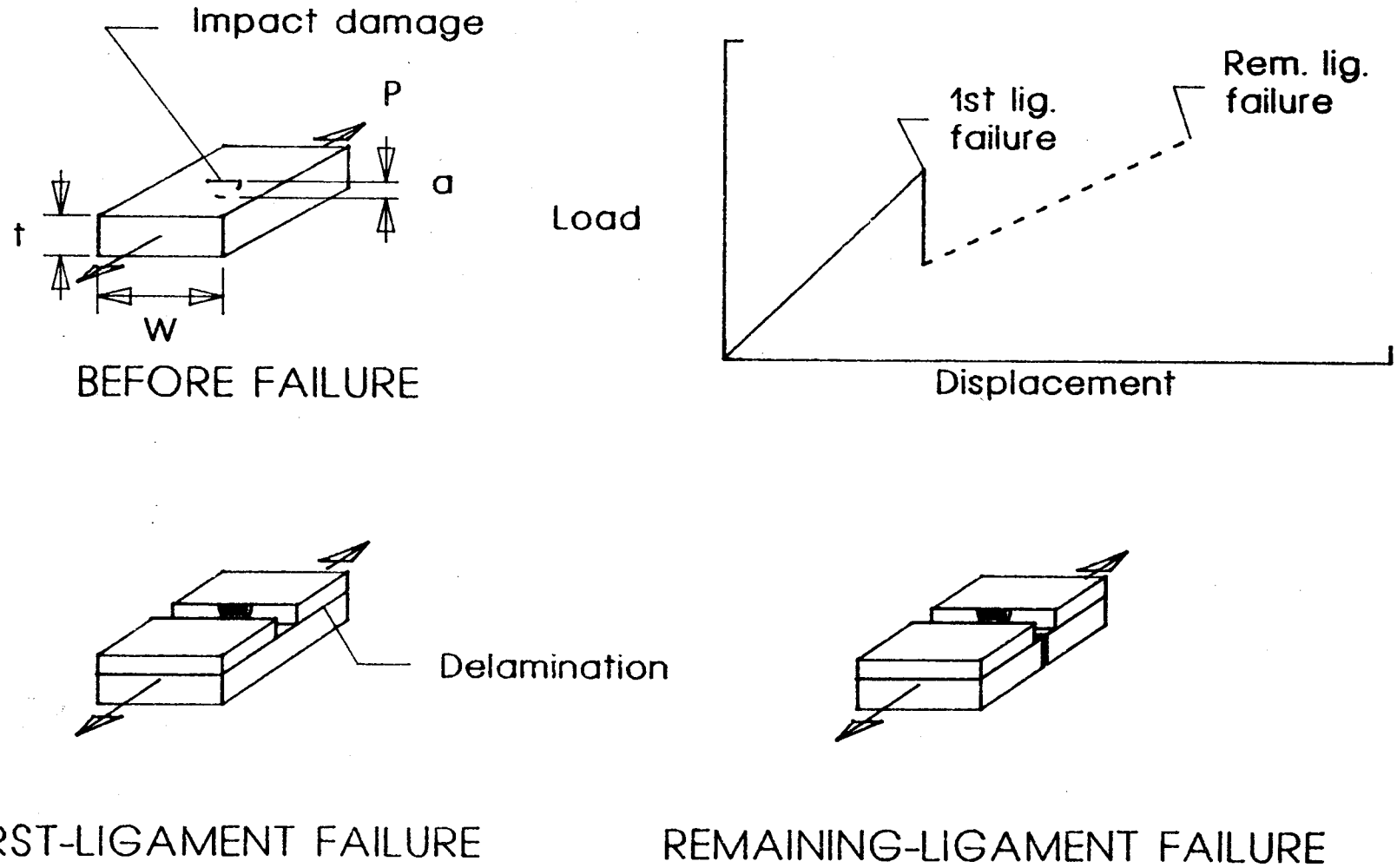

Figure 3.- Two-part failure with impact damage.

FIG3.ASM

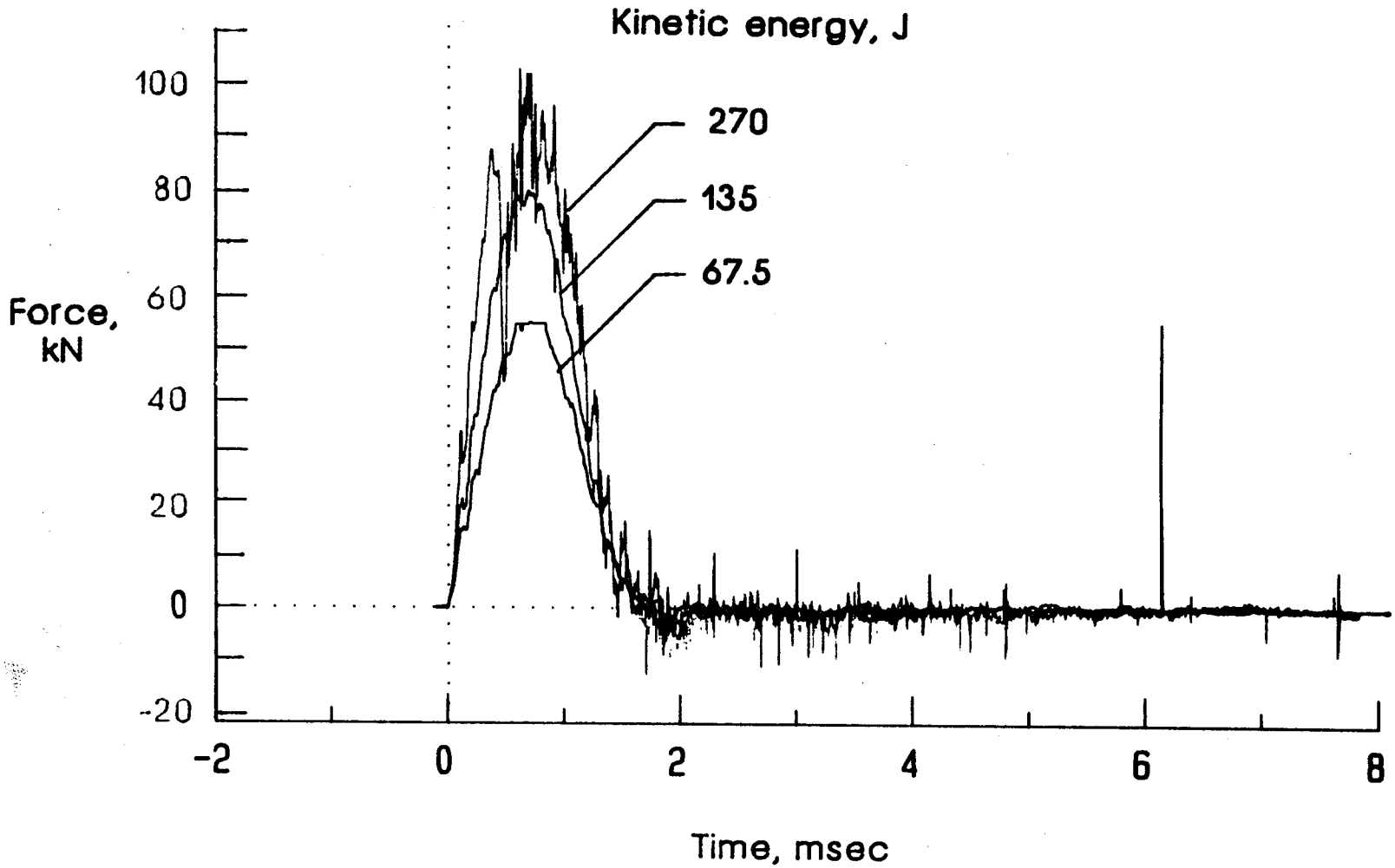

(a) Filled ring.

Figure 4.- Effect of kinetic energy on impact force versus time for 9.0-kg (19.9 lbm) impacter.

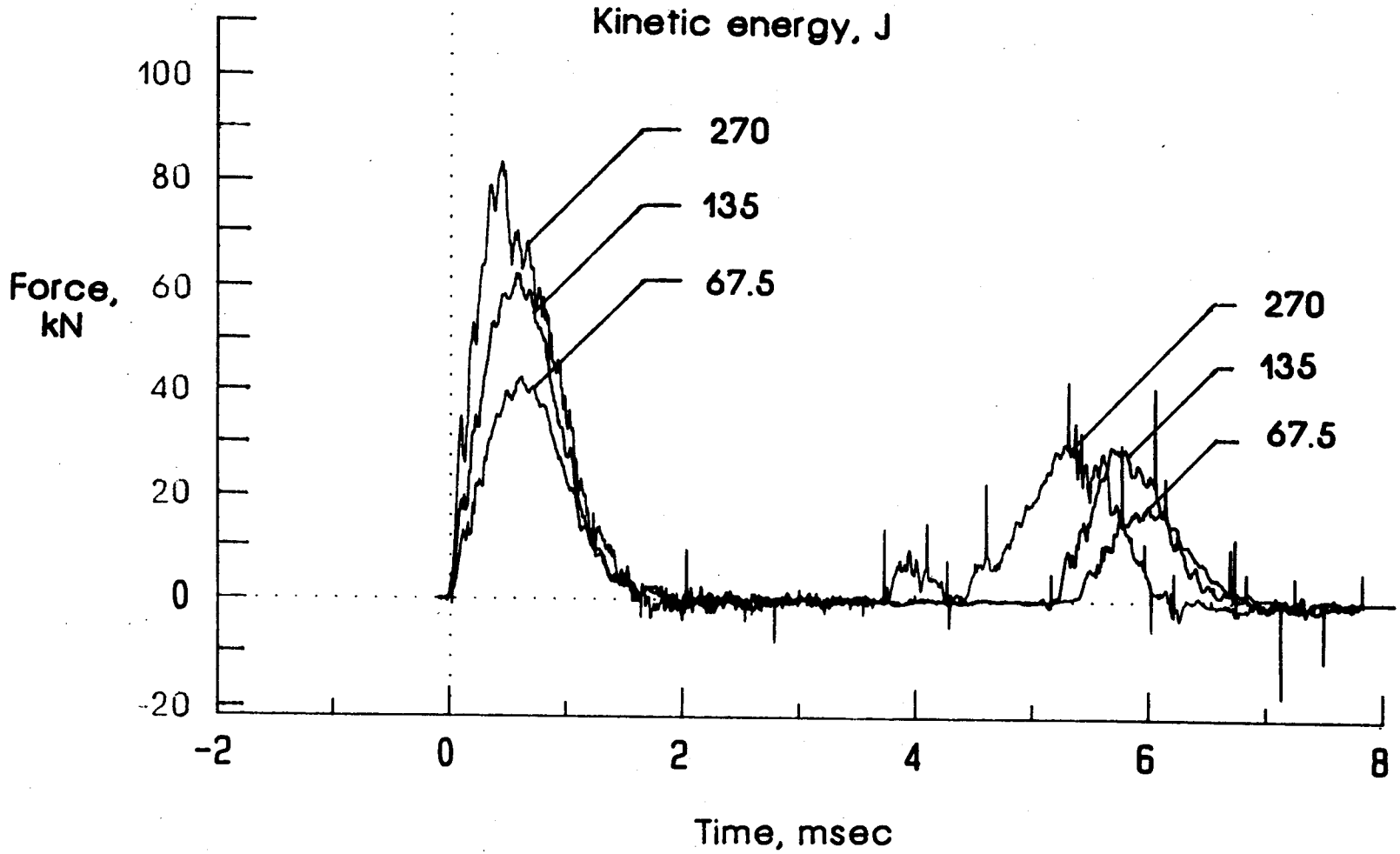

(b) Empty ring.

Figure 4.- Concluded.

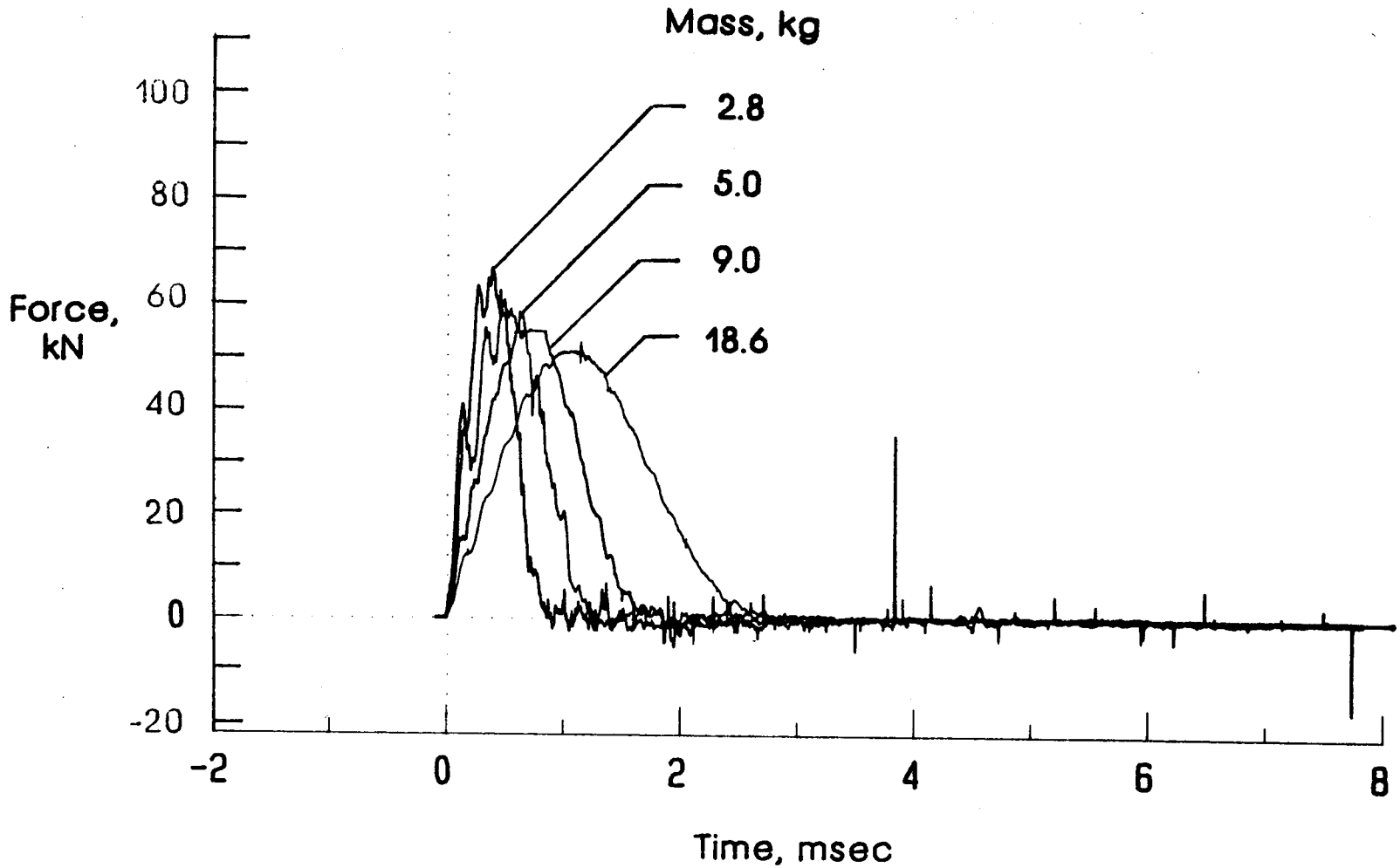

(a) Filled ring, KE = 67.5 J (49.8 ft lbf).

Figure 5.- Effect of impacter mass on impact force versus time.

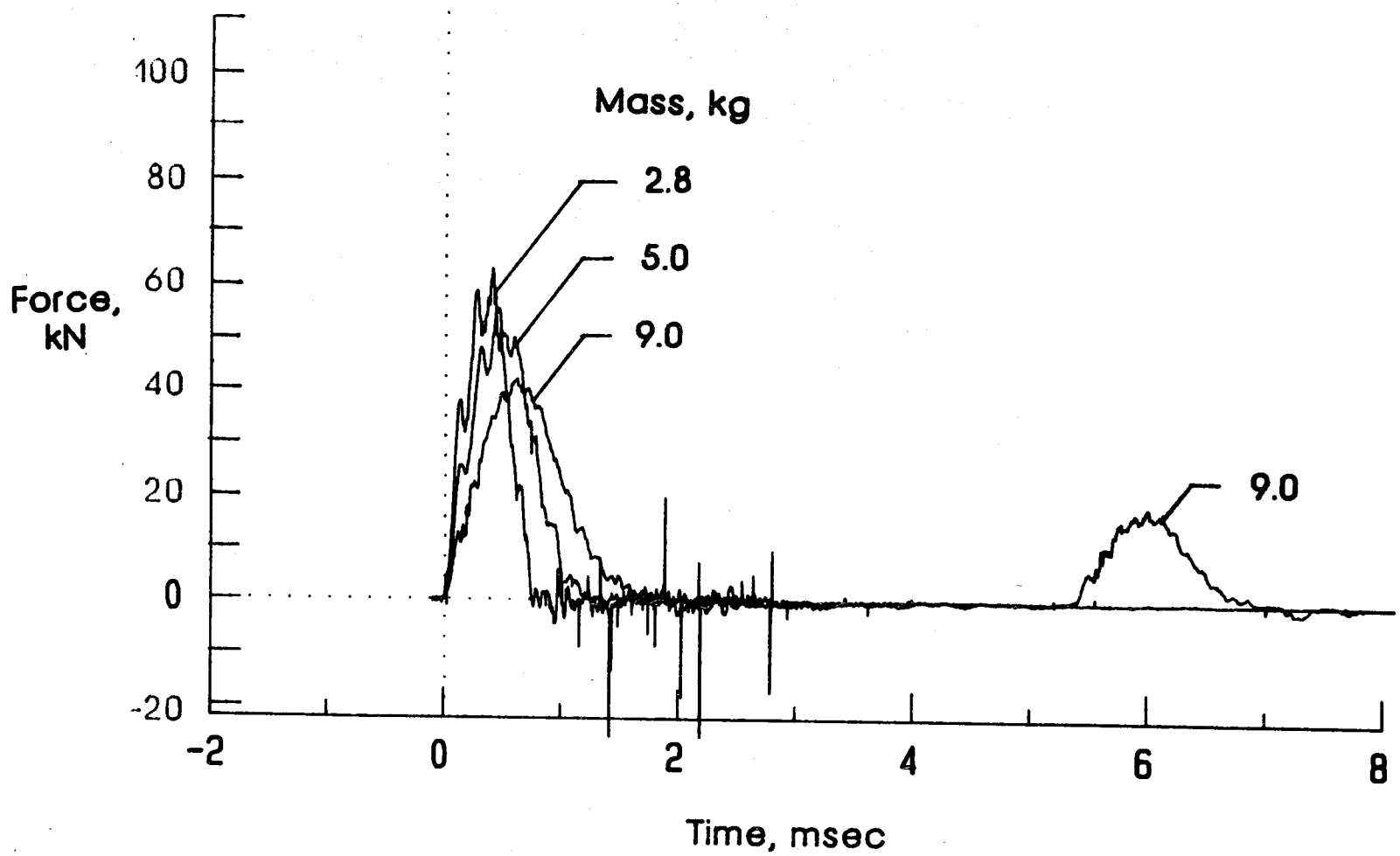

(b) Empty ring, KE = 67.5 J (49.8 ft lbf).

Figure 5.- Continued.

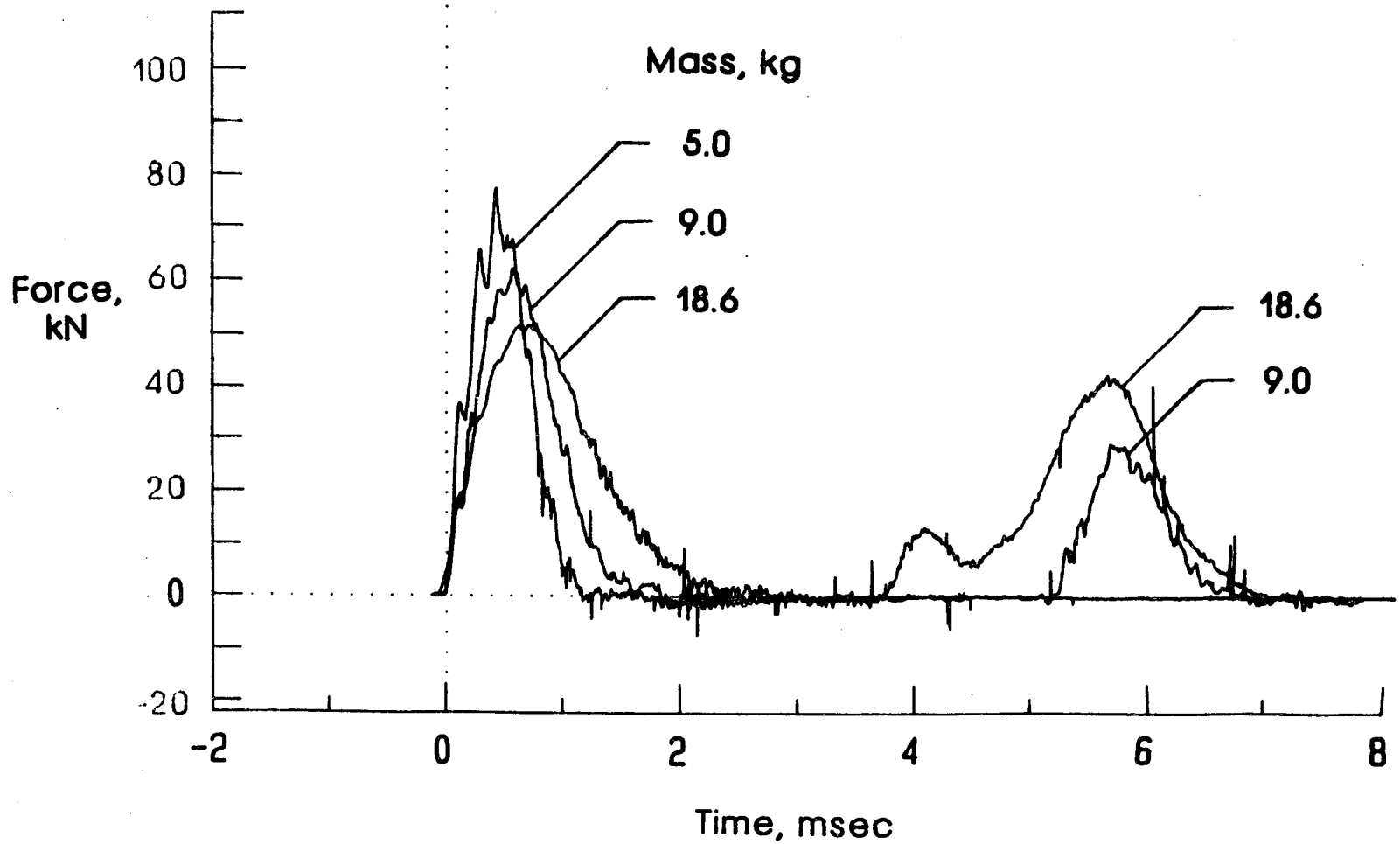

(c) Empty ring, KE = 135 J (99.5 ft lbf).

Figure 5.- Concluded.

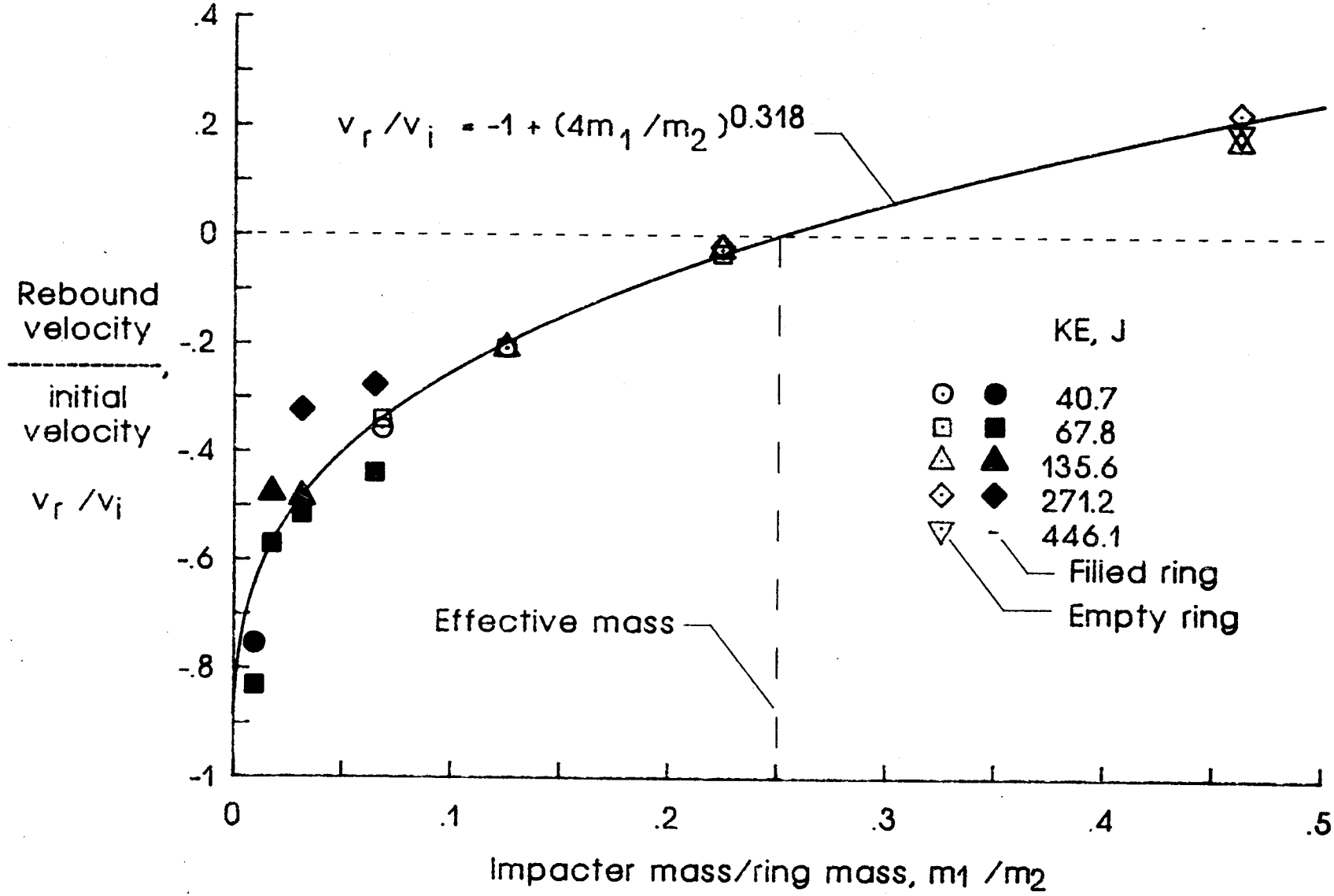

Figure 6.- Rebound velocity versus impacter mass.

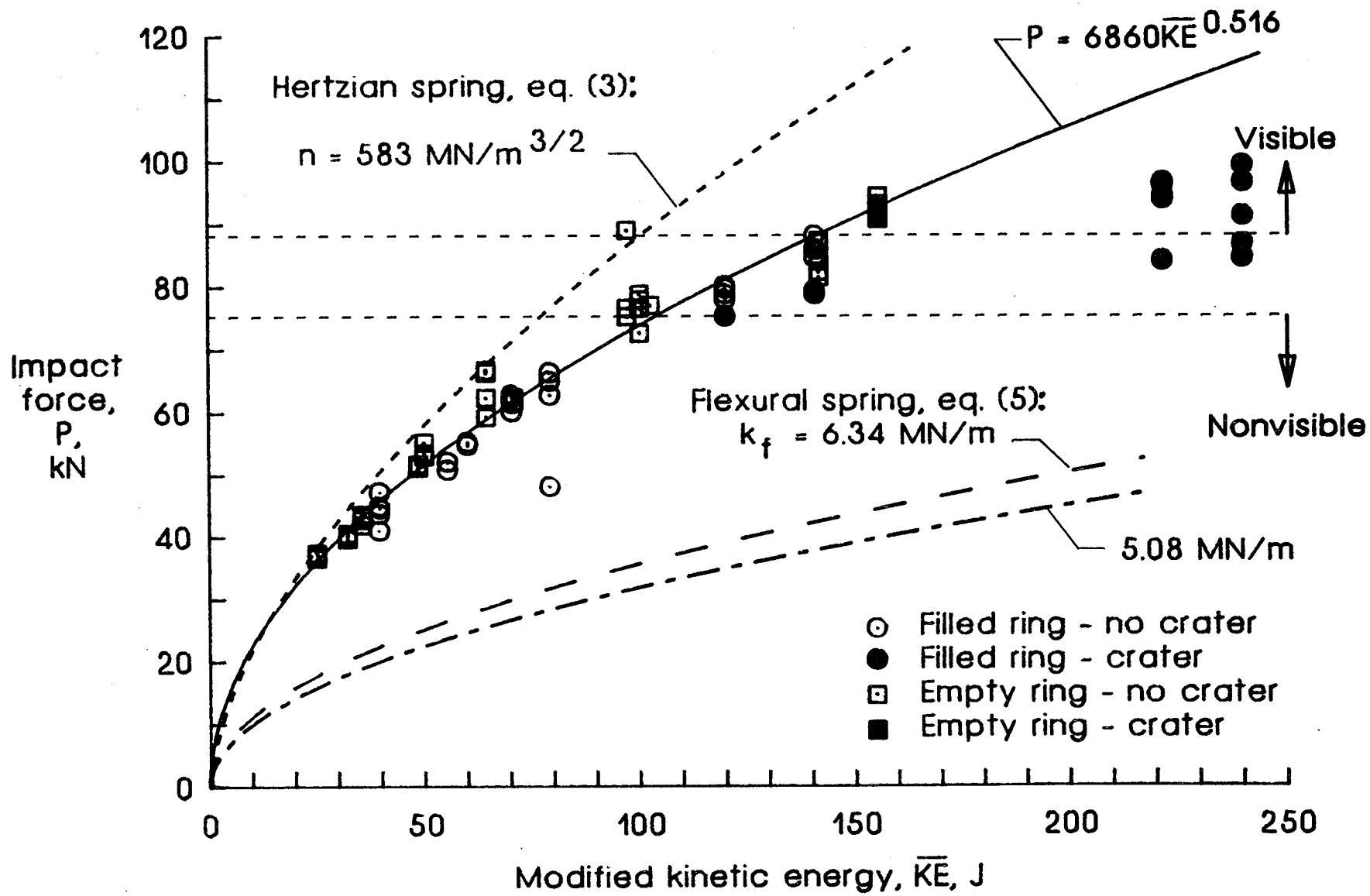

Figure 7.- Impacter force versus modified impacter energy for filled and empty rings. $\overline{m}_2$ = 72.1 and 10.0 kg (89 and 635 lbm), respectively.

FIG6.AST

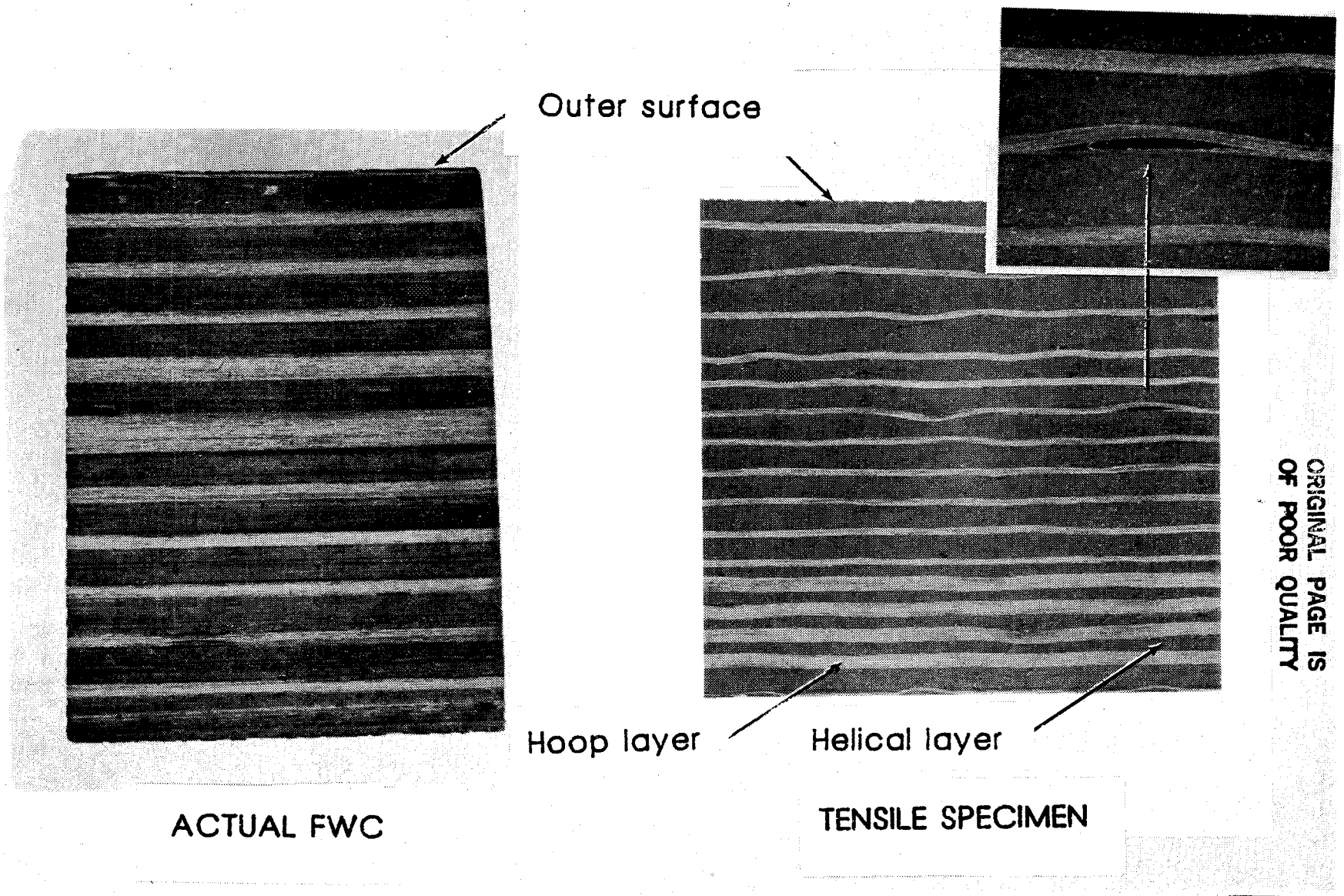

Figure 8.- Photographs of edges of a tensile specimen and a coupon from an actual FWC.

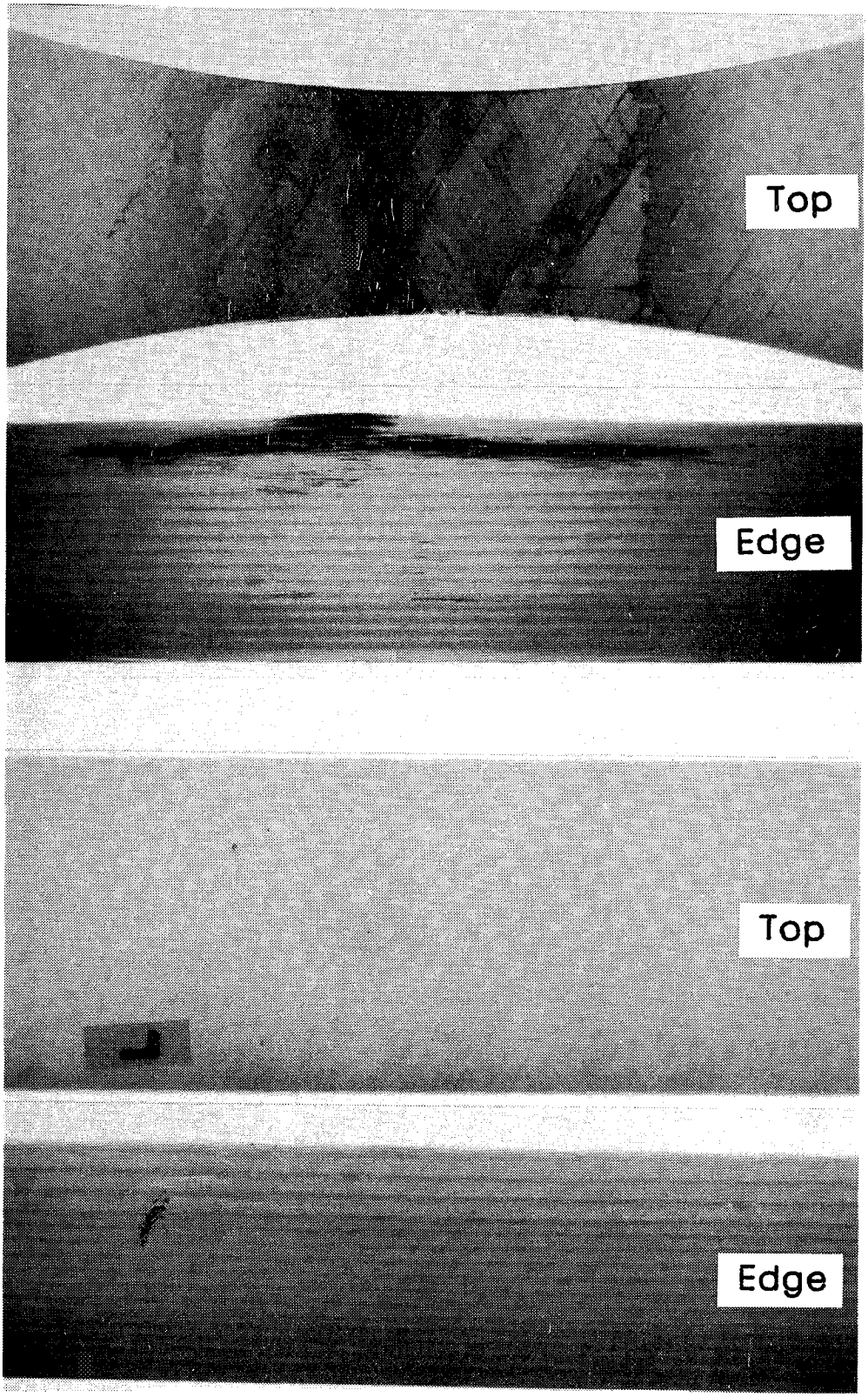

(a) Specimen 7-7, P = 60.0 kN (13.5 lbf).

Figure 9.- Radiographs of first-ligament failure (filled ring).

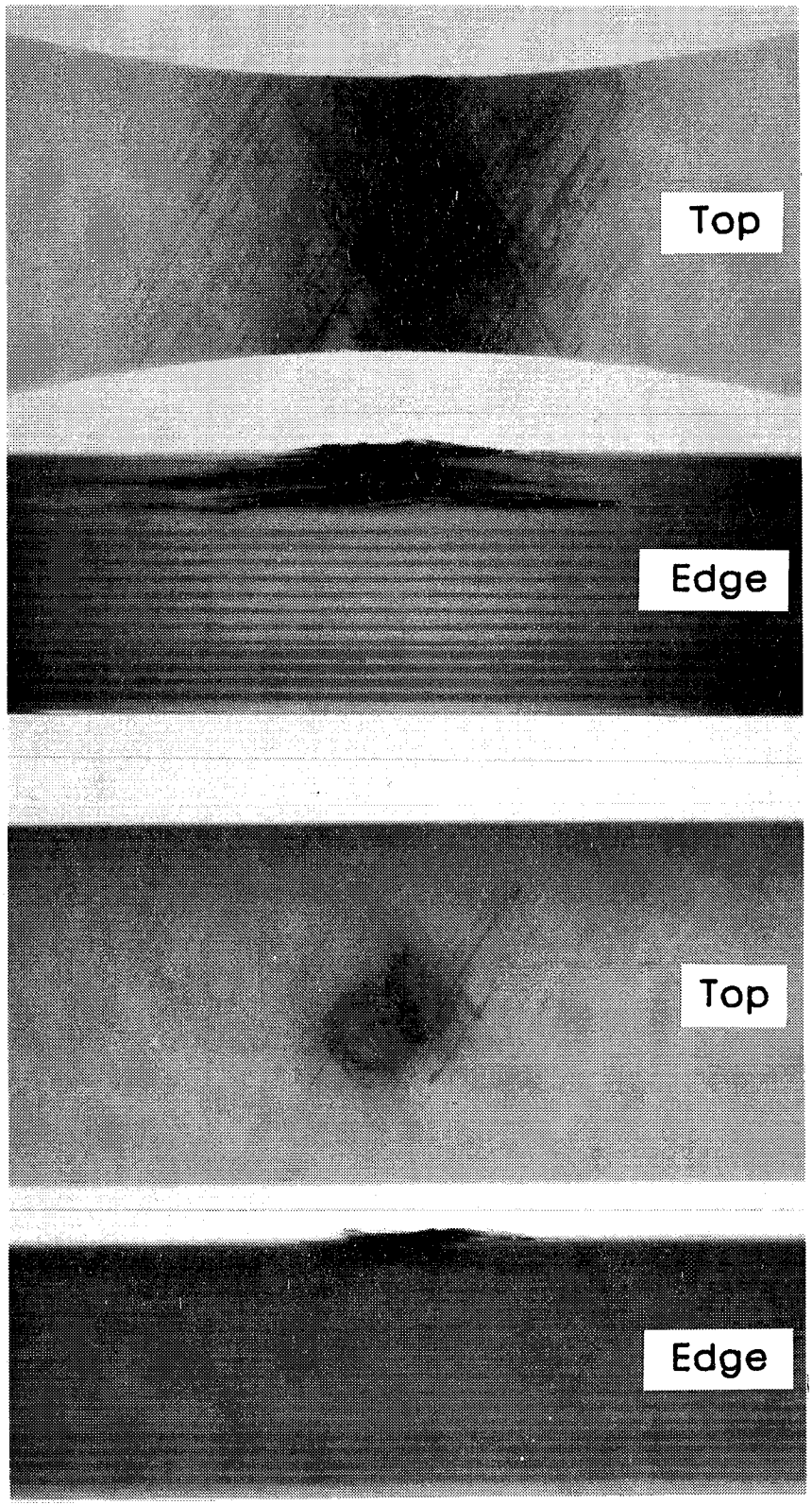

(b) Specimen 7-8, P = 79.2 kN (17.8 lbf).

Figure 9.- Concluded.

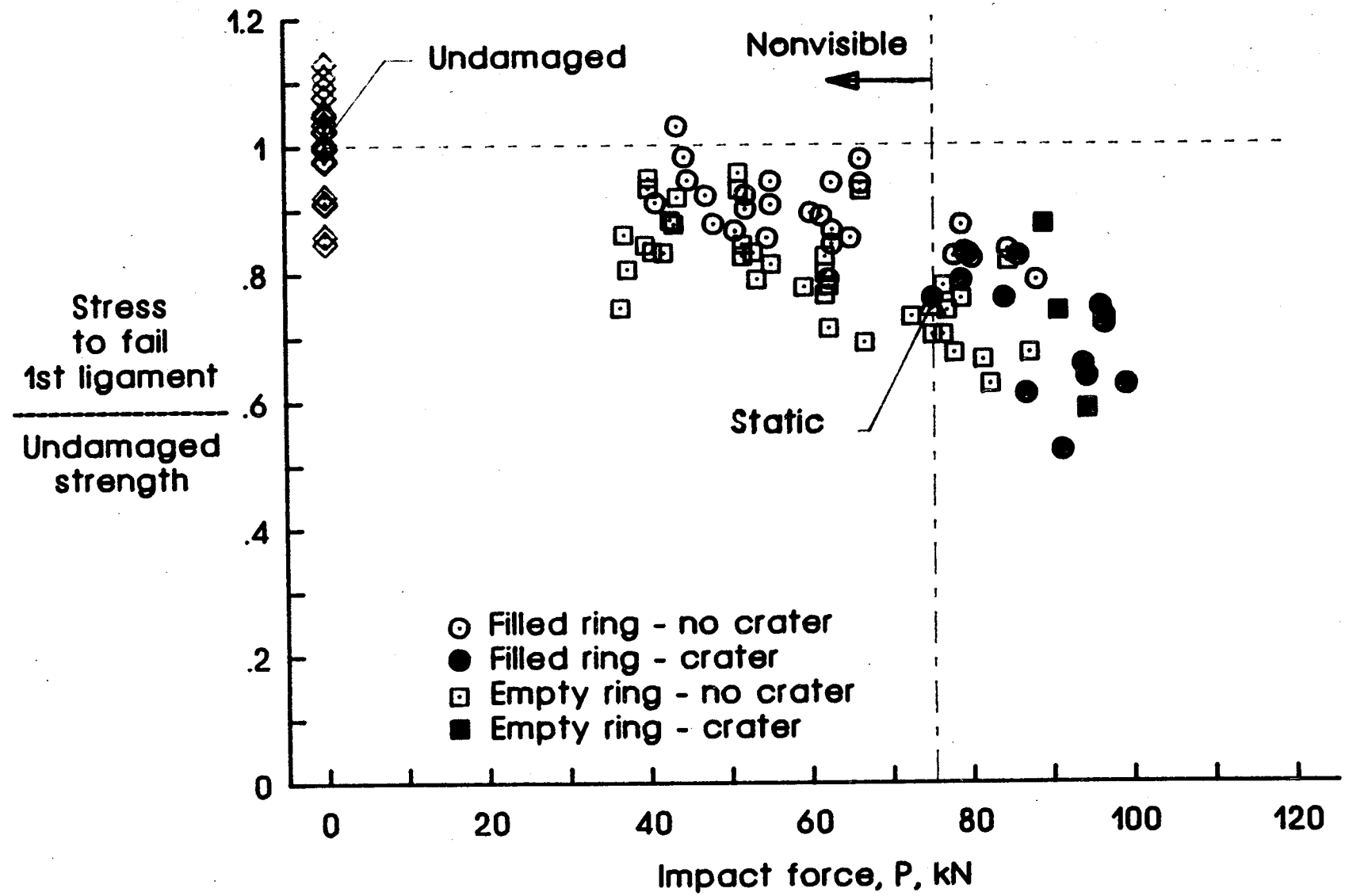

(a) Stress for first-ligament failure.

Figure 10.- Ratio of impact strength to undamaged strength versus impact force.

FIG8A.AST

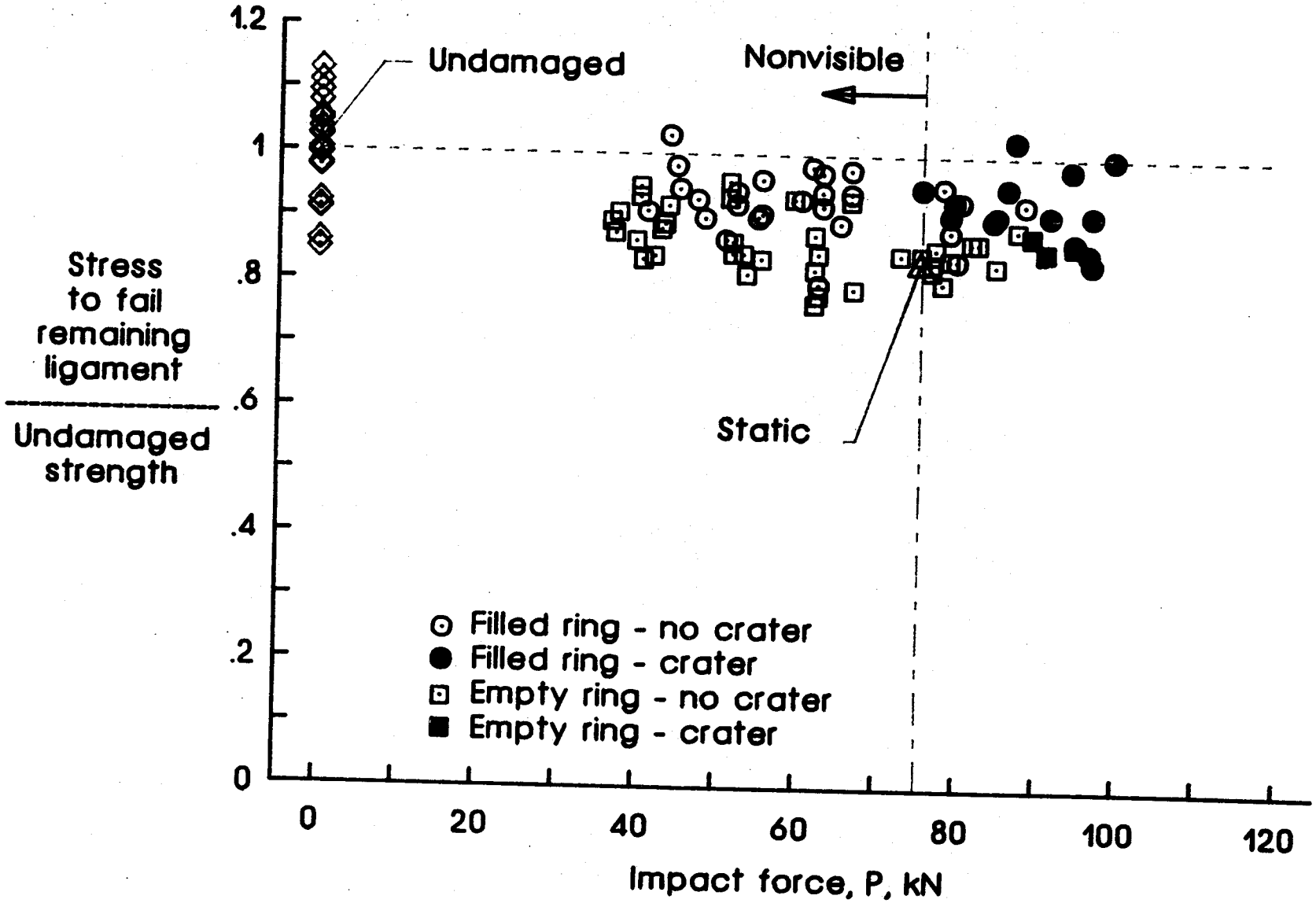

(b) Stress for remaining-ligament failure.

Figure 10.- Concluded.

FIG8B.AST

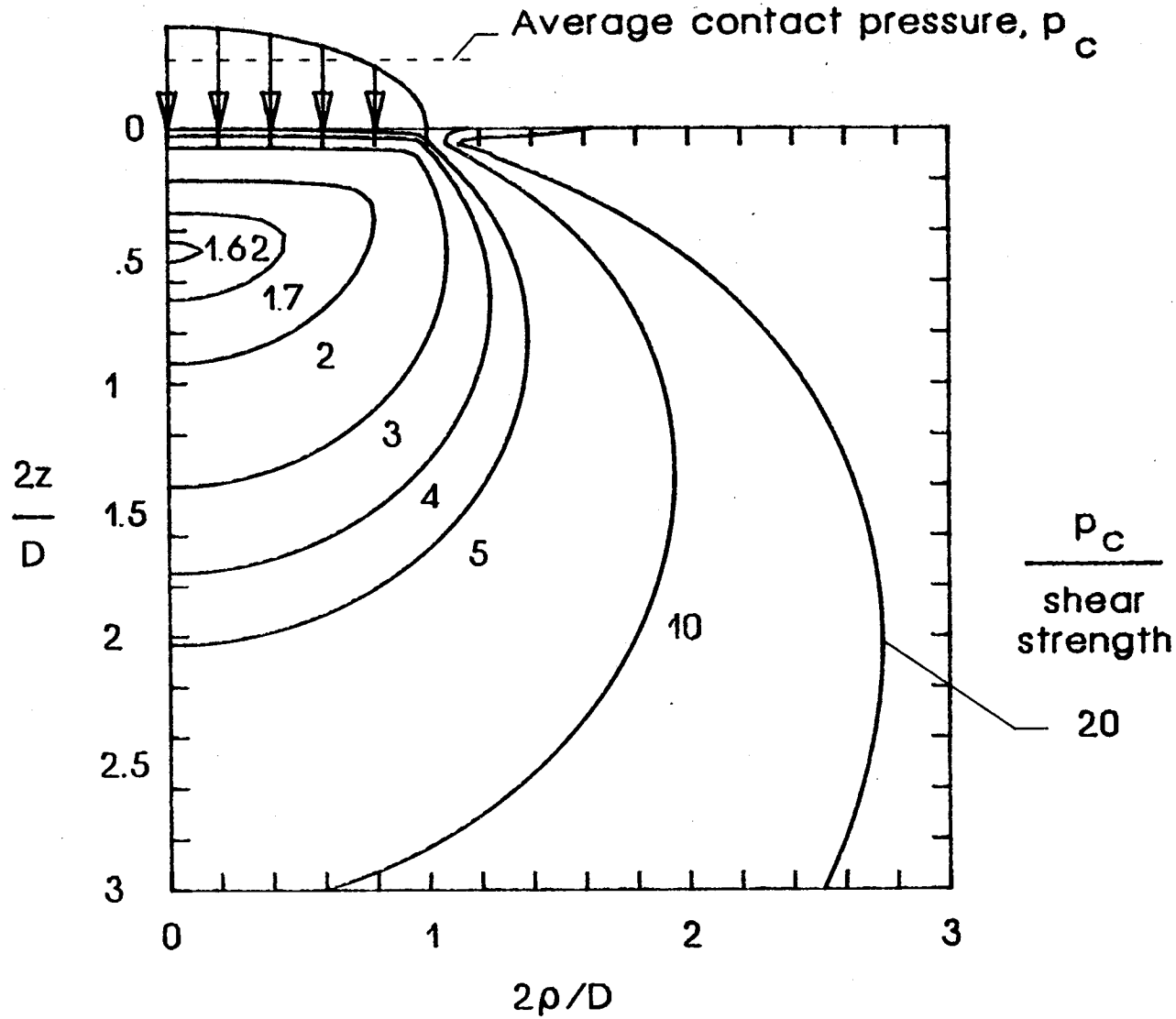

Figure 11.- Damage contours from Love's solution for hemispherical contact pressure.

FIG10.AST

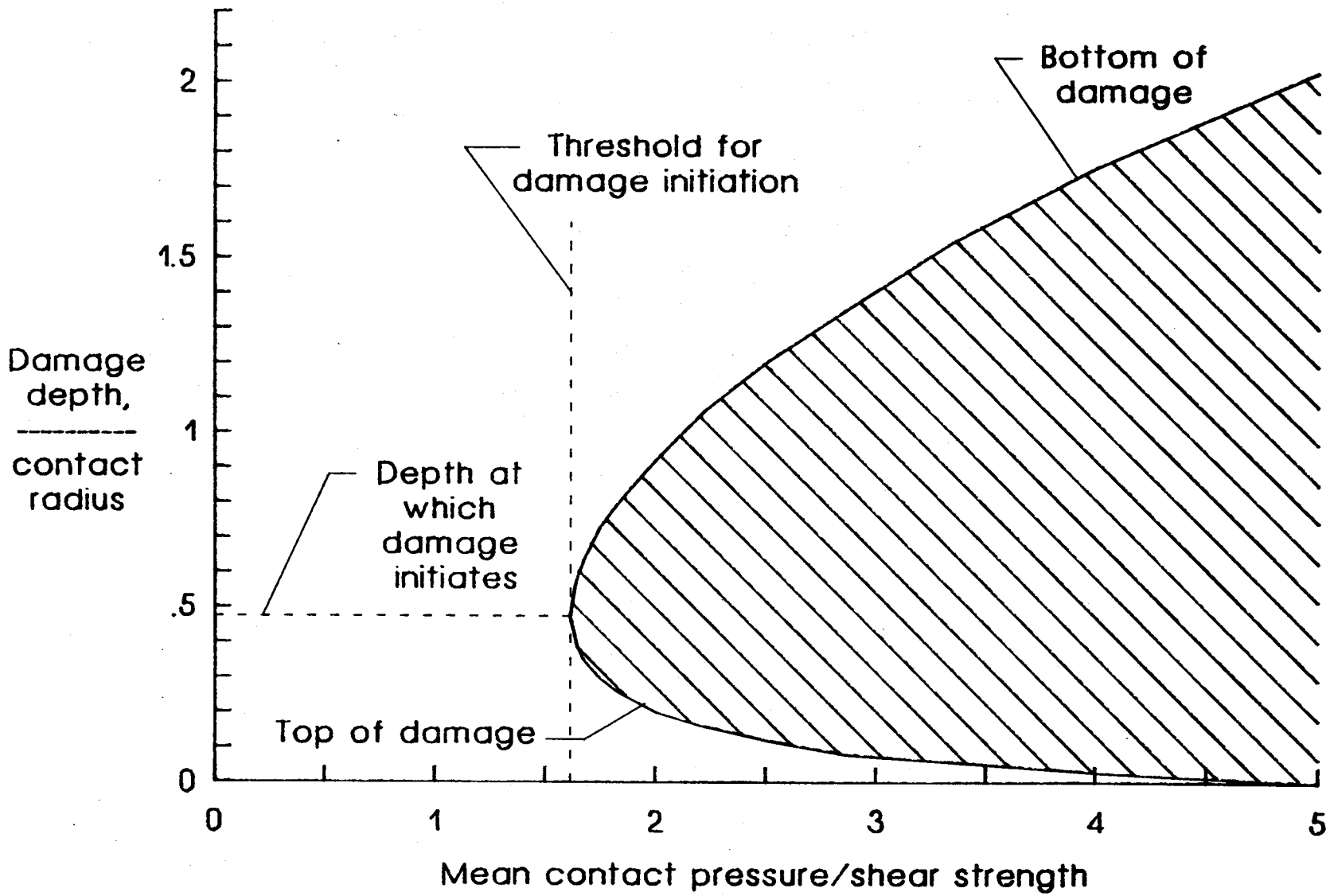

Figure 12.- Damage depth versus mean contact pressure according to Love's solution and principal shear criterion for failure.

FIG11 AST

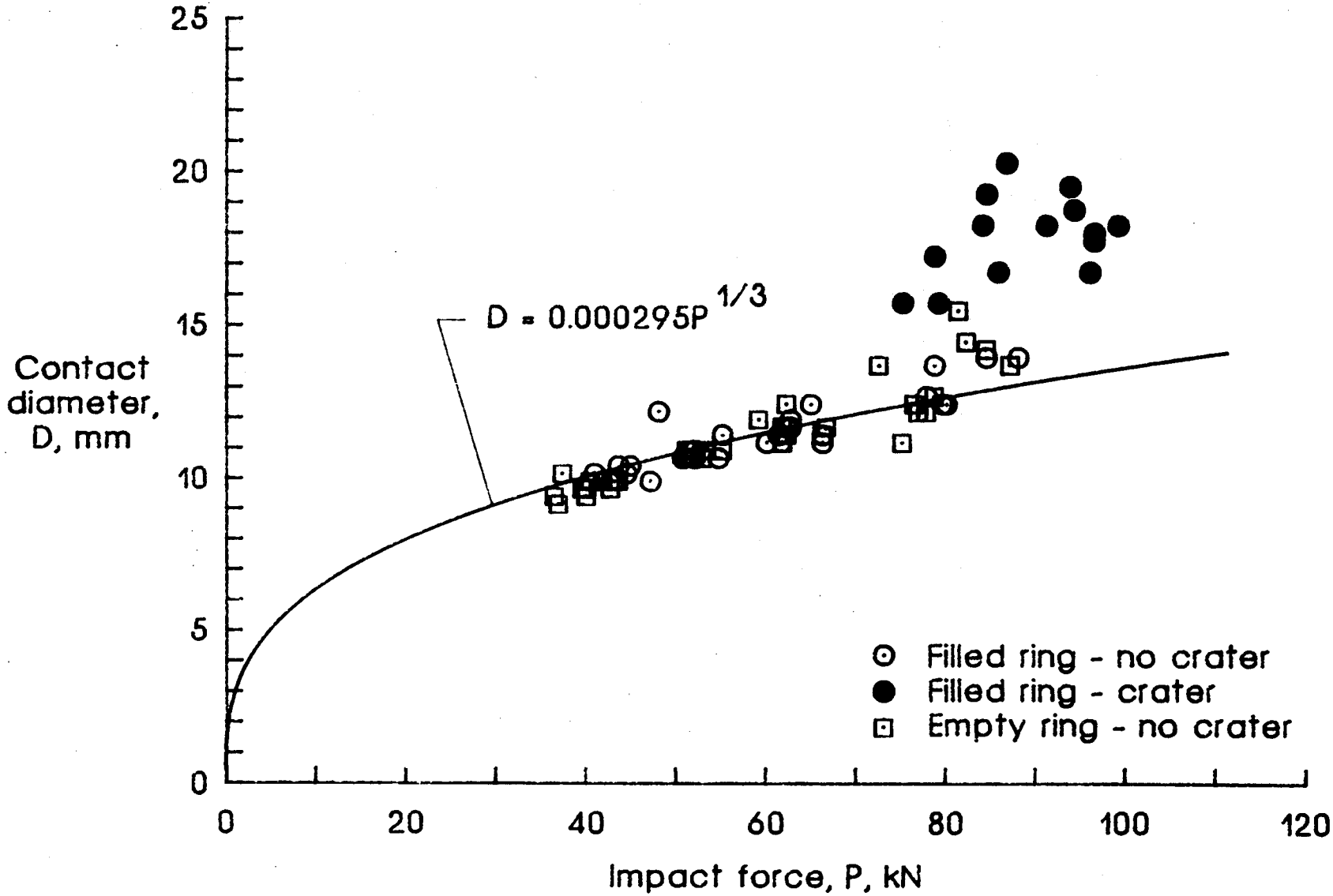

Figure 13.- Contact diameter versus impact force.

FIG11.FWC

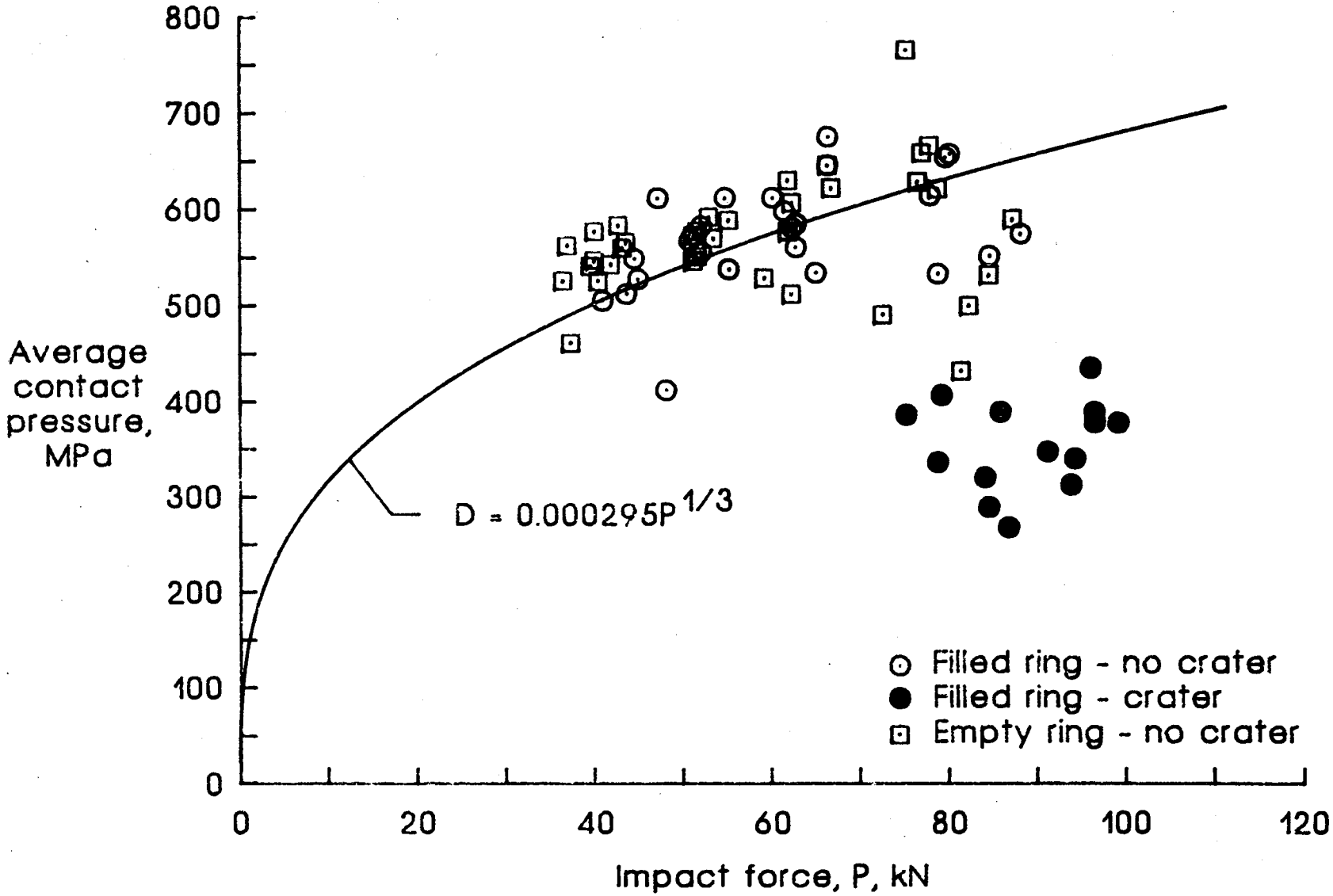

Figure 14.- Average contact pressure versus impact force.

FIG12.FWC

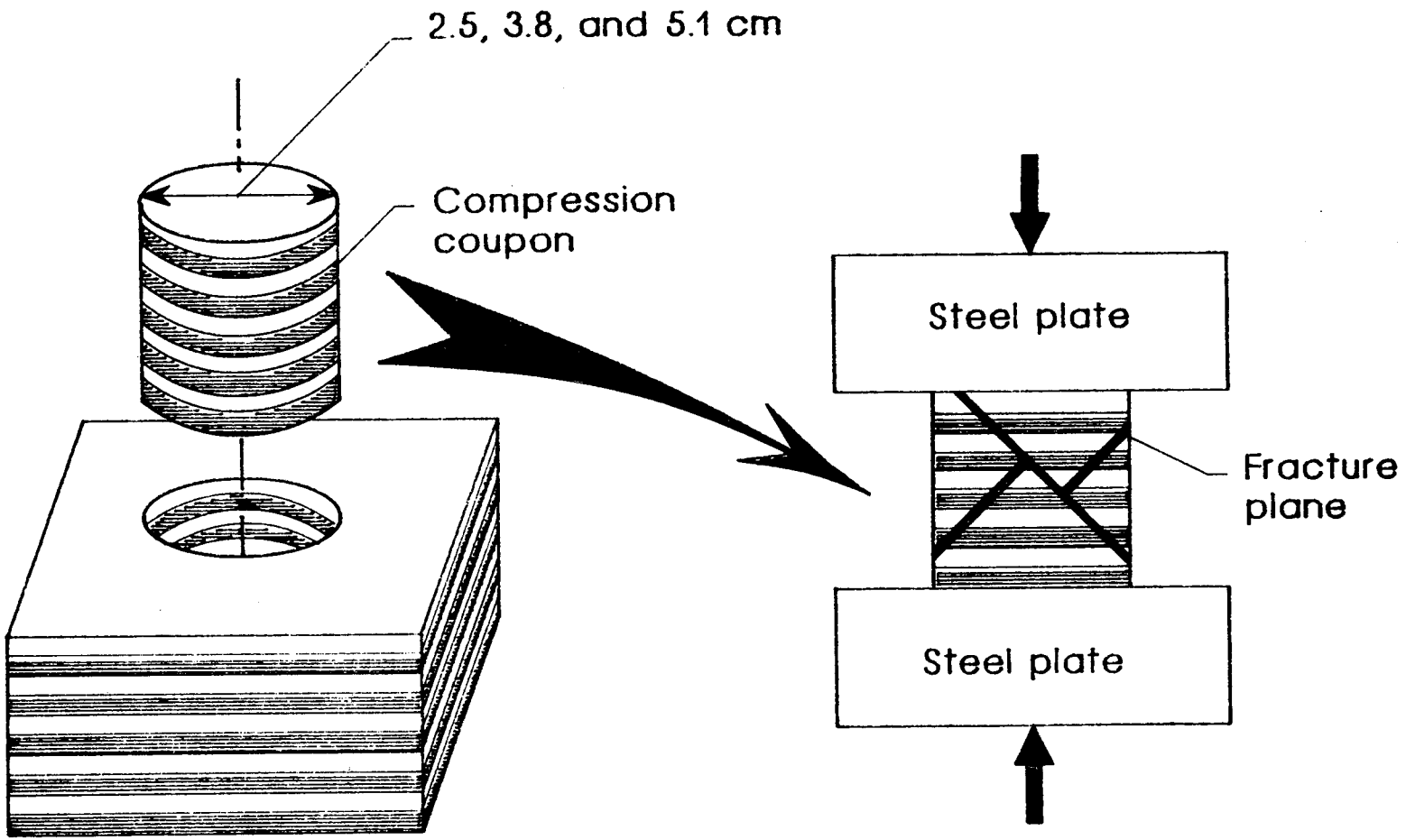

Figure 15.- Compression test for shear strength.

JANNAF FIG15B

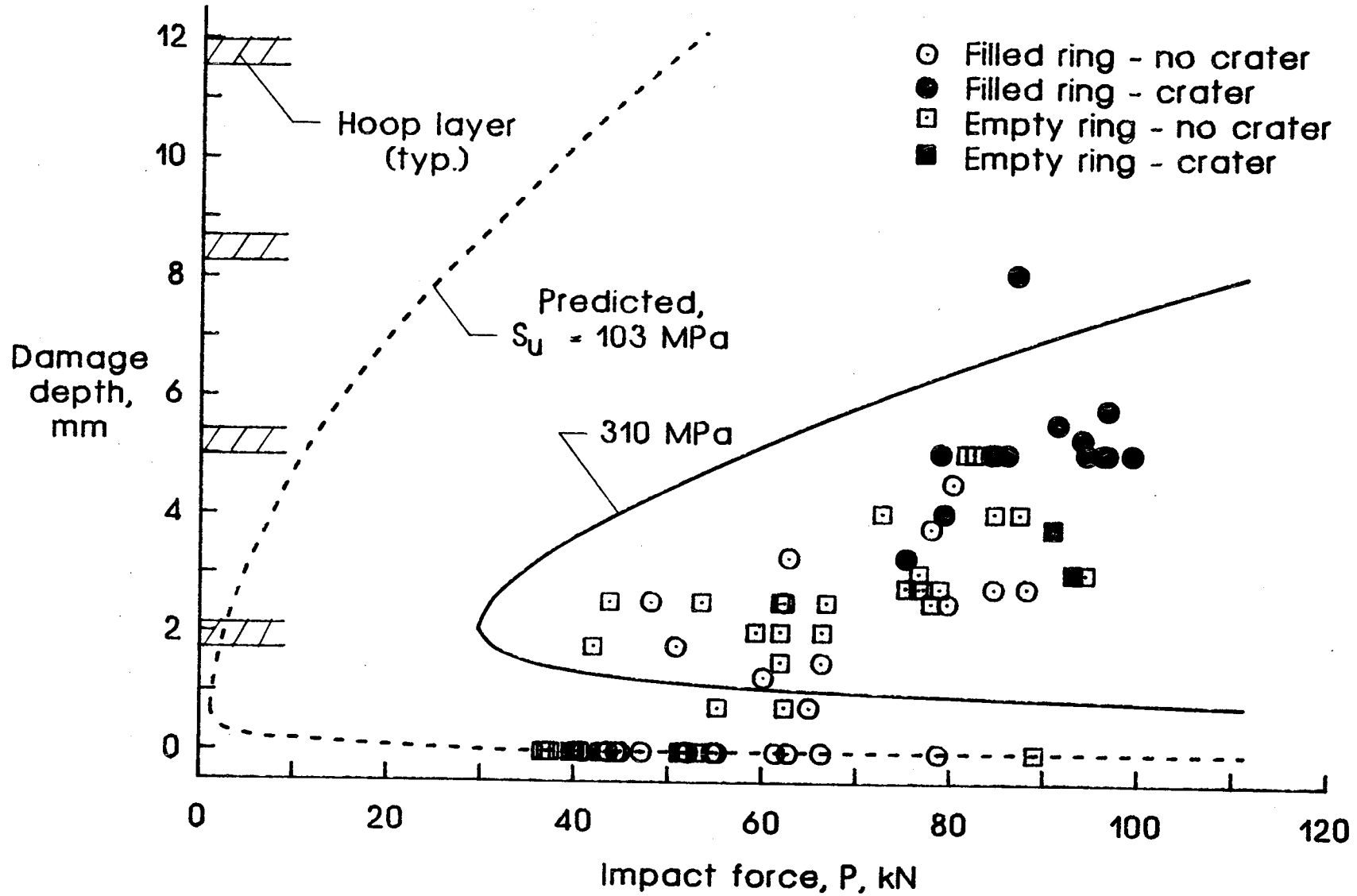

Figure 16.- Comparison of predicted impact damage and radiographs.

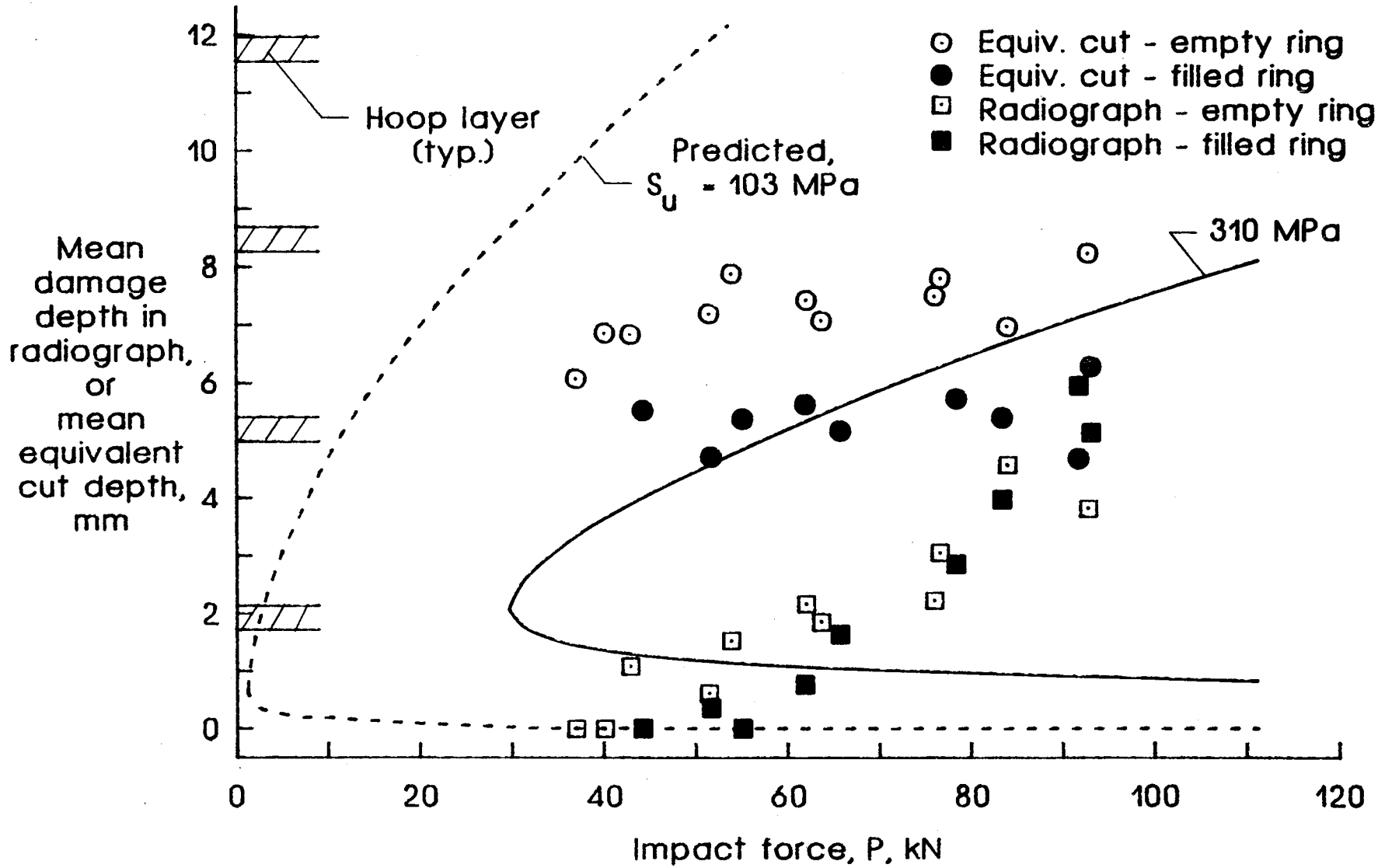

Figure 17.- Comparison of equivalent cut depth and radiographs. (Test values are averages of more than one test.)

FIG15.AST

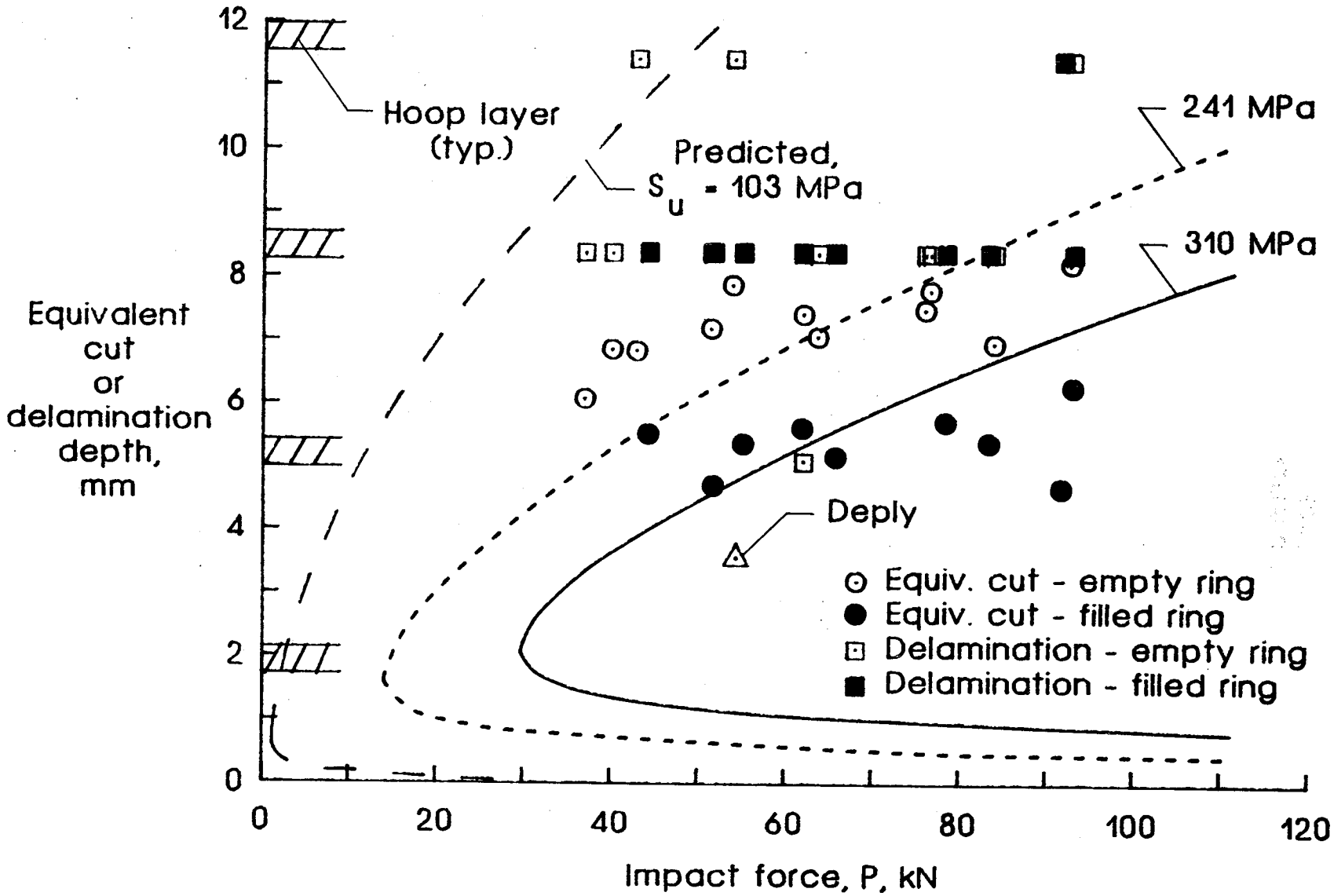

Figure 18.- Comparison of equivalent cut depth and delamination depth. (Test values are averages of more than one test.)

FIG14 A ST

(a) 13X magnification.

(b) 280X magnification.

Figure 19.- Photographs of deepest layer with fibers broken by impact (second helical layer below the outermost hoop layer).

Standard Bibliographic Page

1. Report No.	2. Government Accession No.	3. Recipient's Catalog No.
NASA TM-89099		

4. Title and Subtitle	5. Report Date
STRENGTH OF A THICK GRAPHITE/EPOXY ROCKET MOTOR CASE AFTER IMPACT BY A BLUNT OBJECT	February 1987
	6. Performing Organization Code: 506-43-11-04
7. Author(s): C. C. Poe, Jr. and W. Illg	8. Performing Organization Report No.
9. Performing Organization Name and Address: NASA Langley Research Center, Hampton, VA 23665-5225	10. Work Unit No.
	11. Contract or Grant No.
12. Sponsoring Agency Name and Address: National Aeronautics and Space Administration, Washington, DC 20546	13. Type of Report and Period Covered: Technical Memorandum
	14. Sponsoring Agency Code

15. Supplementary Notes

16. Abstract

NASA is developing graphite/epoxy filament-wound cases (FWC) for the solid rocket motors of the Space Shuttle. They are wet-wound with AS4W graphite fiber and HBRF-55A epoxy. The membrane region is about 36 mm (1.4 in.)[1] thick. A study was made to determine the reduction in strength of the FWC due to accidental damage caused by low-velocity impacts. Two 76.2-cm-diameter (30 in.) by 30.5-cm-long (12 in.) cylinders were impacted every 5 cm (2 in.) of circumference with 1.27-cm-radius (0.50 in.) impacters of various masses. The impacters represented tools and equipment dropped from various heights. One cylinder was empty and the other was filled with inert propellant. Five-cm-wide (2 in.) test specimens were cut from the cylinders. Each was centered on an impact site. The specimens were x-rayed and loaded to failure in uniaxial tension. The strengths and depths of impact damage were analyzed in terms of maximum impact force. Rigid body mechanics and the Hertz law were used to derive an equation for impact force in terms of kinetic energy and the masses of the impacter and target. The depth of damage was predicted in terms of impact force using Love's solution for pressure applied on part of the boundary of a semi-infinite body. The predictions of damage depth were reasonably good. Damage depths increased with increasing impact force, and strengths decreased with increasing impact force, and strengths decreased with increasing impact force. The strengths were reduced by as much as 37 percent without visible surface damage. Even the radiographs did not reveal the non-visible damage.

[1] Original measurements were made in English units.

17. Key Words (Suggested by Authors(s))	18. Distribution Statement
Graphite/epoxy composite Filament winding Motor case Impact damage Residual strength	Unclasified - Unlimited Subject Category - 24

19. Security Classif.(of this report)	20. Security Classif.(of this page)	21. No. of Pages	22. Price
Unclassified	Unclassified	51	A04

For sale by the National Technical Information Service, Springfield, Virginia 22161

NASA Langley Form 63 (June 1985)